Synthesis and characterisation through diffraction techniques of two stable cubic $MAPbI_3$ photovoltaic perovskite phases

Rhianna Day

School of Physical Sciences

University of Kent

Thesis submitted for the degree of MSc Chemistry by Research

Supervisor: Professor Mark Green

Submitted: 18th December 2021
Word Count: 22, 591

Acknowledgments

I would like to express my gratitude to Professor Mark Green for his supervision, guidance and support throughout the project, as well as to Jake Minns who contributed to the numerous refinements of the crystals phases and offered his time and knowledge.

I would also like to thank Dr. Van Beek and his team at The European Synchrotron Radiation Facility (ESRF) for his provision and guidance in carrying out diffraction at the ESRF and SNBL facilities, which were fundamental to the results outlined in this study.

I would like to offer my appreciation to the fellow members of my research group for their motivation and optimism throughout the years.

Abstract

The study aims primarily to explore synthetic routes and chemical manipulation of perovskite materials and characterise these materials through diffraction techniques. This thesis presents the discovery of a new hybrid perovskite structural phase, derived from the prototypical $MAPbI_3$ perovskite, which demonstrates room temperature ordering of the methyl ammonium cation and the presence of interstitial iodine sites through the addition of iodide vapour. Additionally, this thesis presents a stable tetragonal-cubic chemical phase transition in the $MAPbI_3$ perovskite when synthesised using high temperature vacuum assisted annealing.

Table of Contents

Synthesis, Results and Discussion

Conclusions & Future Work

Table of Figures

Abbreviation	Name
$MAPbI_3$	Methyl ammonium lead tri iodide
$MAPbBr_3$	Methyl ammonium lead tri bromide
$MAPbCl_3$	Methyl ammonium lead tri chloride
MA, MA^+	Methyl ammonium, Methyl ammonium cation
PV	Photovoltaic
PCE	Power conversion efficiency
MAI	Methyl ammonium iodide
XRD	X-ray diffraction
PXRD	Powder X-ray diffraction
DFT	Density functional theory
DSSC	Dye sensitised solar cells

Chapter 1: Introduction to Photovoltaic Perovskites

1. The Importance of Development in Renewables

Over the past decade photovoltaic perovskites have gained enormous prevalence in the renewable energy sector. The unique class of perovskites demonstrate an assembly of promising qualities, attributed to both their structural make up and chemical composition, which place them at the forefront of the evolution towards renewable energy alternatives. Photovoltaic solar power has been proclaimed as a viable replacement for fossil fuel consumption, the fundamental driving force of the global warming crisis faced by the world today. Photovoltaic perovskites offer a clean energy alternative, whilst also providing an immediate solution to combat the diminishing supply of fossil fuels which have dominated the energy sector for many decades.

Research into photovoltaic perovskites has been motivated by low production costs and impressive efficiencies – which appear set to rival even the most successful silicon based solar cells by 2030. The family of perovskites possess an array of impressive properties, including ease of fabrication from simple solution synthesis, low carrier recombination rates which facilitate high power conversion efficiencies, strong solar absorption within the UV range and tuneable bad gaps. Photovoltaic perovskite cells have individually reached PCEs as high as 22%, however maximum efficiencies have been seen in silicon-perovskite tandem solar cells, which achieved 28% PCE in 2019. [1] The exponential rise in efficiencies observed over the past ten years make evident that the PV perovskites alone have the capability to rival traditional solar sources. Other recent advancements into PV functionality such as the ability to process thin film PV cells, means photovoltaic perovskites are becoming progressively favourable in the renewable sector.

One of the most extensively explored photovoltaic perovskites is the organohalide perovskite family with the general formula ABX_3, where A is an organic cation, B is a transition metal cation and X is a halogen. The large organic cation sits within a metal-halide framework which is composed of BX_6 octahedra. [1] It is this class of the photovoltaic perovskites – most notably methyl ammonium lead iodide – that have provided some of the most promising results within the field. Power conversion efficiencies in excess of 25% have been observed, which exceeds beyond comparable solar modules such as silicon-based heterojunction devices which have reported efficiencies in excess of 15%. [2] However organohalide perovskite cells are still in their infancy and display a number of factors which are inhibiting their commercialisation. [2] The lack of long term chemical and thermal stability due to impeding factors such as light soaking and thermal stress of the crystallites which comprise the cells is a particular drawback for the long term viability, alongside concerns over the toxicity of the widely incorporated lead (Pb) component. These problems must first be addressed and mitigated before photovoltaic perovskite solar cells can be implemented on a large scale.

1.1. Climate Change

The demand for renewable energy resources was recognised as early as the 1970's when scientists warned that conventional fossil fuel supplies were depleting rapidly, and that alternative sources of energy would be needed in order to sustain the energy consumption of the world. [3] Recently, the need for development of renewables has been further emphasised due to the mounting pressure on governments around the globe to reduce carbon emissions which are accelerating global warming and causing detrimental environmental consequences.

The Greenhouse Effect refers to the natural planetary atmosphere which surrounds the Earth, trapping solar radiation and hence increasing surface temperatures to a level which is sufficient for human existence. Greenhouse gases facilitate this naturally occurring phenomenon. When solar radiation enters the atmosphere it is either absorbed or reflected by the Earth's surface, a proportion of the reflected radiation is absorbed by greenhouse gases in the atmosphere. [4] A large proportion of what is referred to as greenhouse gases consists of water vapour, however carbon dioxide also accounts for a significant contribution, alongside a smaller percentage of triatomic gases such as ozone (O_3) or nitrous oxides (N_xO). Although the greenhouse gases themselves are relatively inefficient at absorbing incoming solar radiation, they are able to

absorb the radiation that is reemitted from the Earth as longwave radiation (4-100 μm). [4] The triatomic structure of the common greenhouse gases allows them to capture radiation in the thermal infrared spectrum more efficiently than linear gaseous molecules which are more abundant in the atmosphere, such as oxygen (O_2) or nitrogen dioxide (NO_2), making them superior at retaining thermal energy and hence maintaining a habitable temperature on Earth. Despite the natural occurrence of the Greenhouse Effect, when it is coupled with anthropogenic emissions it becomes problematic.

Over the past century, the global population has increased at an unprecedented rate. Technological advancements have seen the world become increasingly globalised, and with this, electricity and fuel consumption has increased simultaneously. In 2020 the World Energy Council reported that the world population is approaching 8 billion, and that electricity production had spiked to an all-time high of 23,000 TW per hour. [3] As a direct consequence of the exponential increase in energy consumption and human generated emissions during the 20th and 21st century, unprecedented greenhouse gas accumulation in the Earth's atmosphere has forced global temperatures a point which exceeds the Earth's natural variability. [5]

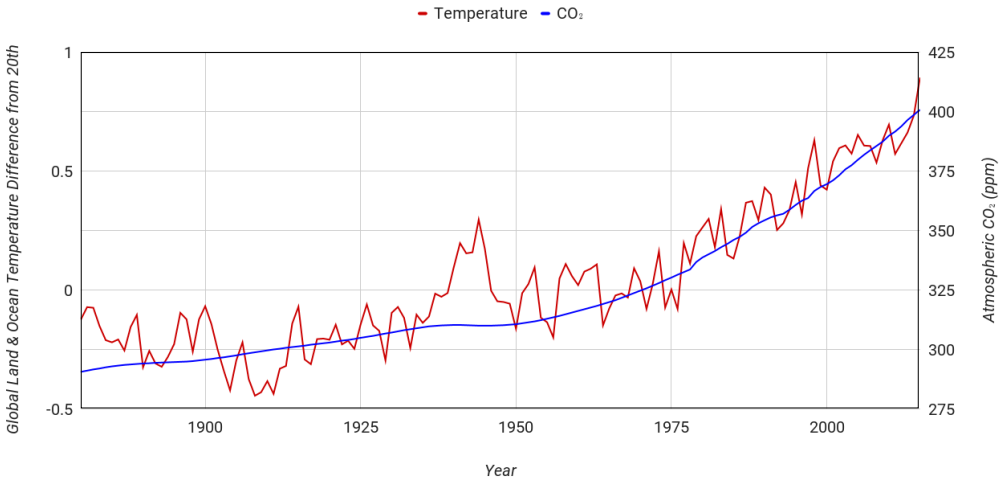

Figure 1. Variation in global land and ocean temperature associated with the increase in CO_2 concentration since the 20th century. [5][6]

The subsequent acceleration of climate change has already demonstrated a catalogue of harmful consequences around the globe, most evidently rising sea levels as a secondary effect of the rapid reduction of glacial ice caps alongside increased occurrences of natural disasters, destruction of ecosystems and concerning effects for agricultural production.

Not only do these consequences threaten the longevity and health of the planet, but they also pose direct threats to human life such as food insecurity, higher prevalence of disease and submersion of land. World leaders and energy companies alike have quickly realised the extent and magnitude of global warming effects, and the urgent need for renewable energy in order to mitigate the problem. Most recently climate change summits such as COP26 have been hosted across the world, and a push for large emission generating commercial companies, such as Google, to become more sustainable or be held accountable has become an emerging trend. As a result, development of renewable energy sources has been pushed to the forefront of the scientific research field.

1.2. Renewable Energy

In order to successfully mitigate the global climate change problem there are three main routes which can be considered; reducing the demand of fossil fuels, developing clean and renewable alternatives for fossil fuels and improving general energy efficiency. The most imperative of which remains the development of low emission, alternate energy sources that will allow countries and economies to continue to thrive whilst also combating climate change and the detrimental environmental impacts it presents. At present, worldwide energy production is dominated by the three culprit fossil fuels oil, gas and coal. However, renewable sources have gained outstanding leverage over recent years and are undergoing continuous improvements to facilitate large-scale production. Oil remains the world's primary source of energy, accounting for over a third of the total consumption, closely proceeded by natural gas and coal. [3] Nevertheless renewables such as hydropower, bioenergy, solar, geothermal and wind energy offer alternative supplies with significantly reduced carbon emission output. It is evident that renewable sources are becoming progressively more prominent, and it is predicted that by 2040 the global energy mix will have increased from 25% to 40% of renewable energy alternatives. Within the same timeframe half of electricity generation will be produced exclusively from low-emission sources. [7]

Currently, bioenergy and hydropower are dominating the renewable energy sector. Remarkably, bioenergy accounted for 9.5% of the total global energy supply in 2019. [3] In 2016, hydropower accounted for a staggering 71% of the total renewable electricity usage, wind power and solar energy accounted for 7% and 1% respectively. [3] Despite a low utilisation

rate – at 2.5% on average of domestic electricity generation in 2019 – solar PV is still emerging as a likely competitor for fossil fuels in the future. The benefits of high efficiency potential and low cost production place the renewable energy source as an excellent alterative.[3]

The global energy mix is transitioning to incorporate cleaner and more sustainable energy sources, however the movement is much slower than is needed in order to mitigate the impending climate change crisis. These slow advancements can be attributed to many factors, as each renewable presents individual advantages and drawbacks. In the ideal scenario, by 2100 the global energy mix will look similar to the predictions outlined in Figure 2, with a heavy reliance on solar resources and reduced demand for gas and coal in particular.

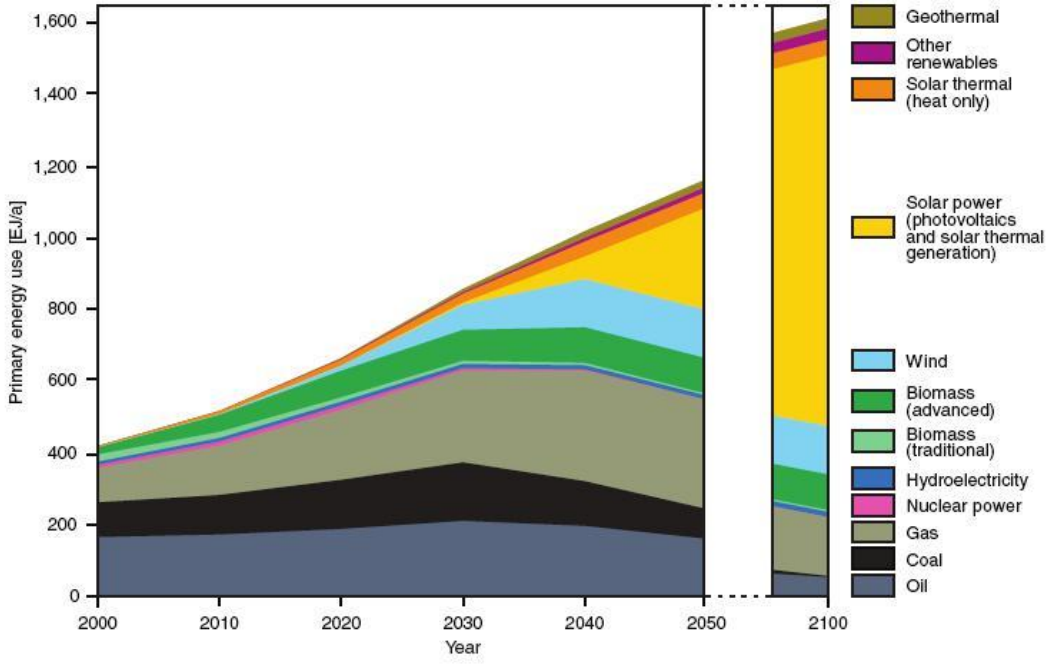

Figure 2. Predictions of the global energy transition 2000-2050, with declining fossil fuels and incorporation of more renewable resources into the energy mix. [8]

1.2.1. Hydropower

Hydroelectric power is generated via the conversion of kinetic energy of water reserves to electrical energy and has proven to be hugely successful as an alternative energy supply. Hydropower is commonly generated from a static water source such a reservoir or dam yet in

recent years, developments have meant that 'run of river' power can also be produced, whereby the kinetic energy from a river current is used to drive a turbine and generate electricity. This method ensures that even in locations where water is not in surplus it is still possible to generate hydropower. Hydropower offers additional benefits such as water sustainability, capacity to store potential energy and cost effectiveness. The undeveloped potential for hydropower is estimated to be 10,000 TWh per year.[3] Hydropower is currently deployed in over 160 countries, yet high start-up costs and lack of adequate infrastructure are hindering the success of the renewable, especially in developing regions such as Africa which has a huge unfulfilled potential. More affluent regions, particularly Asia, are successfully utilising their hydro resources with 35% of installed hydropower capacity. [8] Despite the success of hydroelectric power thus far it is limited as an alternative supply in regions which are plagued with water insecurity, and with drought and irregular weather cycles becoming more frequent around the world, it raises concerns over the reliability of hydroelectric sources.

1.2.2. Wind Energy

Wind energy is not as widespread as hydropower, but is generated in a similar way, transforming kinetic energy produced via wind to power the movement of turbines and hence generate electricity. Wind energy offers huge potential as demonstrated in Denmark which produced 42% of the entire country's energy supply through wind turbines in 2012.[3] Despite the apparent success of wind power plants, they have faced backlash from local communities over the physical appearance and, much like hydropower, the initial expenditure poses difficulties for the start-up of these facilities. Wind power plants can be limited by inconsistent wind speeds, especially when located on-shore, due to this, a surge of off-shore turbines has been observed. Off-shore turbines are able to achieve superior wind speeds for greater efficiency and hence cleaner energy which proves promising for future prospects of wind farms. However, the traditional turbine infrastructure requires development in order to increase energy output capacity which at present is inhibiting the viability of the renewable on a large scale.

1.2.3. Geothermal Energy

Geothermal energy is natural heat radiated from the Earth's core via the movement of magma. It can be used directly for heat energy or used indirectly to produce steam to be transformed into electrical energy. Geothermal reservoirs can be naturally occurring or constructed by drilling into specifically located hot rocks. Extensive geologic mapping and deep well drilling is often required for extraction. Drilling processes present a risk of increased seismic activity, which can be a concern in regions with increased tectonic sensitivity. At present, geothermal energy offers the greatest capacity for energy output, with an estimated 430 million EJ stored within the initial 3 km depths of the Earth's crust. [9] Despite the abundance of geothermal energy, the time and cost of locating and extracting reserves means that the resource is not used to its full potential in all regions.

Although this renewable energy alternative is vastly underexploited, countries such as Iceland are successfully fulfilling 50% of their energy demand via geothermal resources. [3] Alongside China, Iceland have led the way for geothermal energy. Iceland have promoted geothermal heat pumps as a substitute for domestic heating systems, which account for 150-230 kWh/m^2 in residential buildings annually, and employ geothermal resources for industrial processes. [9] Geothermal pumps offers both a clean and inexpensive method compared to conventional natural gas boiler systems which output 308 g/kWh and 453 g/kWh of CO_2 emissions respectively.[9] The disparity in carbon output between the respective energy sources emphasises the need to combat carbon emissions and equally the success that small-scale approaches can have on mitigating the problem.

1.2.4. Bioenergy

Bioenergy is produced from organic matter referred to as biomass. Biomass absorbs solar energy which is converted and stored as chemical energy, it possesses an array of application ranging from ethanol and biodiesel fuel production to combustion to generate electrical energy. Traditionally biomass was used for heat energy, which is still the case in some developing countries, however more recently, the primary use is fuel in the form of liquid or gas for transportation. Ethanol fuel which is produced from fermentation of sugar cane crops has become the most popular and widely used, commonly utilised in Brazil. Many variations of

biofuels are available and more innovations within the sector are emerging for instance recent developments in cellulosic ethanol.

With transportation being a key contributor to global carbon emissions, a green energy source such as biomass, that is capable of providing a replacement for petroleum based fuels, has the potential to have a significant impact on reducing such emissions. When combusted, biofuels have a 41% reduction in carbon emission output compared with traditional fossil fuels. [10] Yet bioenergy is not at present a viable large-scale replacement for fossil fuels due to its low conversion efficiencies relative to diesel and petroleum. Bioenergy does not conventionally fit as a renewable and may be referred to as a 'negative emission technology'. Zero net emissions are achieved as although generating electrical energy via combustion of biomass outputs emissions into the atmosphere, the organic matter which constitutes biomass is photosynthetic, cycling the carbon emission that is output.

1.2.5. Solar Energy

Solar energy is the most abundant power source available on Earth. The sun emits solar radiation, of which approximately 60% reaches the Earth, contributing the equivalent of 1.08×10^{14} kW energy output.[8] This output drastically outweighs the Earths total energy capacity, emphasising the enormous potential of solar radiation. Yet despite this, in 2016 solar contributed a minute proportion, at just 1% of the global energy mix.[3]

Solar energy is driven by an inexhaustible supply of freely available solar radiation and can be transferred to many forms including thermal energy, solar fuels and photovoltaic power. Photovoltaic technologies in particular are rapidly advancing. The World Energy Council predicts that by the 22nd century photovoltaic solar power will dominate the energy sector, accounting for 70% of world's energy supply.[8] Both Germany and China are leading the way for solar based renewables, having already heavily invested in installation of solar technologies. Solar energy does unfortunately have a location dependency; the potential for solar energy varies between countries by geographical location and the irradiance of that area. Although most regions will remain unaffected by the variance, the potential in arctic regions is substantially limited.

Most solar technologies are facilitated by a conventional solar cell, consisting of semiconducting layers connected in series to form a panel which can be incorporated in to buildings, appliances or transportation. When sunlight is incident upon the panels photons of light are absorbed by the solar cells within and converted into electrical energy. Achieving high power conversion efficiencies has, in the past, proven difficult for solar technologies and inhibited the growth of the solar sector of renewables. However, due to development of photovoltaic solar energy and increasing investment in the area, high efficiencies have proven attainable. The renewable has gained attention from countries across the globe, including the US and China, with the International Energy Association predicting solar PV to become the lowest cost energy option. Solar power is rapidly emerging as the renewable energy of choice for large-scale implementation in an attempt to mitigate climate change.

1.3. Basic Solar Cell Construct

The basic function of a solar cell is to transform incident light into an electrical energy supply. Most conventional solar cells work on the basis that photons of light hit the solar device, and in the case they possess enough energy to overcome a threshold, an electron is ejected from the valence band into the conduction band, via a mechanism described by the band-gap theory.

The threshold of the material is related to the binding energy (E_g) of a valence electron, and it is the band gap between the conduction and valence bands that determines the minimum energy required for electron promotion. [11] When the threshold is met, the valence electron is excited from its former state, generating a free negatively charged electron and a 'hole' with an associated 'positive' charge subsequent to the absence of the electron – essentially known as an electron-hole pair. [11] This mechanism is facilitated by the p-n junction, as outlined in Figure 3, which can be considered the most fundamental component of the cell. The p-n junction is established between a positively and negatively doped semiconductor within the device. [11] If the electron-hole pair occurs in the depletion layer then the intrinsic electric field of the solar cell will independently transport the electron to the n-junction and the hole to the p-junction, creating a voltage potential which can be used to drive a current and hence harness the ability to produce energy.

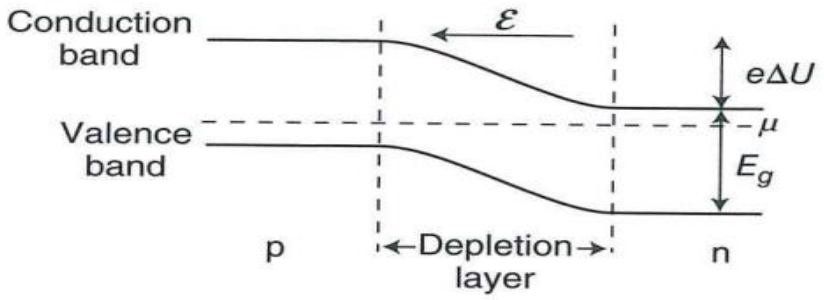

Figure 3. Schematic representation of the formation of a p-n junction, which works via separating carrier pairs in the depletion region to create a voltage potential.[11]

1.3.1. Semiconductor Materials

Semiconductors have laid the foundations for some of the greatest innovations in solid state science in the 20th century and continue to be incorporated into new technologies such as transistors, diodes and solar devices. A semiconductor is defined as a solid which at 0 K possess a chemical potential that is of an energy where the density of states is equal to zero.[12] Unlike metals, the density of states is not finite within a semiconductor. [11][12] A semiconductor has a density of states with an absolute band gap between the highest occupied and lowest unoccupied states, which correspond to the valence and conduction band respectively. The energy of the band gap in a semiconductor (E_g) must be adequately small (~3 eV) that an electron can be excited from the valence band to the conduction band. [11] In the instance that an electron is excited, then the generation of an electron-hole charge carrier pair occurs, and an electrical charge can be generated.

Silicon is one of the most utilised semiconductors in material science, and has been used extensively in emerging solid state technologies due to its optimal semiconducting functionality. Silicon is an example of an intrinsic semiconductor hence it does not have sufficiently high enough concentrations of intrinsic charge carriers to give adequate conduction at ambient temperatures without the aid of doping agents.[13] Doping of semi-conductive materials is a method commonly used where small amounts of electrically active impurities are added in order to enhance the carrier density of the material.[13] This may be achieved via two routes; addition of donor atoms which contribute free electrons to the conduction band or addition of acceptor atoms which uptake electrons from the valence band thereby generating

more holes. These approaches are referred to as n-type doping and p-type doping respectively. For n-type doping it is essential that the introduced electron has a low enough binding energy so that it can be involved in excitations.[13] Both methods achieve increased concentrations of mobile charge carriers, improving current flow and conductivity within the material. [11] Doped silicon possess the desired p-n junction required in an extrinsic semiconductor.

1.3.2. p-n Junction

The p-n junction is ubiquitous in semiconducting and optoelectronic devices. It is generated when a p-type semiconductor and n-type semiconductor are connected, yielding a depletion zone between them.[13] When the solar cell device is incident to photons of light, electron-hole pairs are generated on the condition that the photon has energy greater than E_g.[11] This enables the free electrons and the holes, with an assumed charge of e^+, to migrate freely through the cell. The distance that the charge carriers are able to diffuse through the cell is limited by their excitation lifetime and charge carrier mobility, once their diffusion path length is reached the charge carriers are forced to recombine. This spontaneous recombination of charge carriers is referred to as re-annihilation.[11][13]

All forms of carrier recombination, which may be radiative or via the Auger process, limits the generation of the electric current and therefore decreases the conductivity and efficiency of the cell.[11] In order to generate electrical energy, free charge carriers must be separated before they have an opportunity to recombine.[13] The depletion zone of the p-n junction possess a net electrical charge that can prevent electrons from passing across the junction, as a result, electrons migrate towards the electrode of the n-type semiconductor whilst the holes are free to pass across to the p-type semiconductor.[11] This creates the net flow of electrons responsible for the electric current generated by a semiconducting device. [14] Semiconductive materials are incorporated into an array of optoelectrical devices including solar cell devices, which all function via the p-n junction.

1.3.3. Solar Cell Efficiency Limits

In order to develop a solar cell which is feasible for large-scale implementation it must conform to three essential specifications – high power conversion efficiency, low-cost manufacture and

long lifetime. The efficiency of a solar cell is defined as the electrical energy output divided by the solar energy initially irradiated upon the cell, and is dictated by the band gap of the material.[11] The achievable efficiency of a solar cell has been quantified by the Detailed Balance Limit, more commonly known as the Shockley-Queisser Limit, which determined the highest achievable efficiencies over a single p-n junction to be ~33.7%.[14] The model works based on two assumptions; that photons with an energy greater than the band gap (E_g) have a quantum efficiency of 100% and that all recombination pathways can be reduced to zero, with the exception of radiative recombination.[15] The theory hence concludes radiative recombination mechanism to be the defining factor of the upper limit of minority charge carriers.[15]

It is widely accepted that efficiency limits are associated with the band gap of the solar cell. If we consider a free electron within the n-type band, which has been excited, it will have an energy exceeding the conduction band maximum. However, due to scattering of neighbouring electrons the free electron rapidly loses energy and consequently has an energy closer to the conduction band maximum. The same applies to the hole on the p-type band, hence the energy difference between the carriers decreases, and can not exceed the band gap of the material. It is this energy difference which is output to produce current. Effectively, a semiconductor material with a narrow band gap will have a small output of energy to the external circuit. However, if the band gap is large then there is less sufficient energy available to generate electron-hole pairs thus a compromise between both extremes will allow for optimum efficiency. It is therefore possible to tune the band gap, and in turn the efficiency, depending on the materials within the solar cell.[11]

1.3.4. Conventional Silicon-based Solar Cells

The photovoltaic effect was first realised by Becquerel in 1839, yet the first solar cell was not constructed until 1873 when Fitts used selenium as the primary component and yielded a PCE of just 1%.[16] The practical application of solar devices was not achieved until after 1941 when Ohl produced and patented the first silicon solar device. Silicon solar cells were quickly developed to demonstrate PCEs of 15% within the first ten years, and further advancements have allowed PCEs in excess of 26% to be seen today.[16]

The conventional silicon-based solar cell was designed to maximise efficiency. The solar device itself is composed of a transparent anti-reflective layer above two amorphous silicon layers, forming the p-n junction. The n-type layer is strongly doped, whilst the p-type layer is very weakly doped, in order to encourage the separation of electron-hole pairs.[11] When the charge carriers become free they migrate to contacts at opposite ends of the cell, thus driving a current. The presence of conductive contacts in the design of a silicon solar cell has been known to hinder the efficiency of the solar device, as the front contact occupies a portion of the transparent surface area used to absorb light. The metal contacts at are used to drive a current through an external load, as illustrated below.[11]

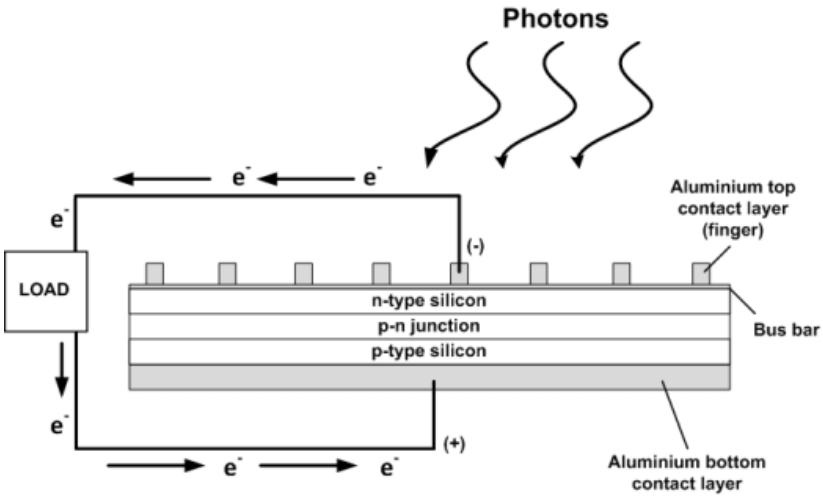

Figure 4. Schematic diagram of a traditional silicon-based solar cell device.[16]

1.3.5. History and Development of Solar Devices

Traditional solar cells are largely composed of silicon due to its optimised semiconducting properties and the closely matched band gap of silicon with the solar spectrum. The potential for solar cells became apparent following Ohls initial movement towards silicon solar devices, when Chaplin observed an efficiency of 6% over a single p-n junction in 1954.[17] Since then it has been seen that silicon solar cells can achieve efficiencies in excess of 26%, although this is significantly lower in commercial solar products.[11][17]

First-generation solar cells were manufactured using monocrystalline silicon, using a production method that involves cutting individual layers from a large single crystal and assembling them together in a grid to produce a panel. These solar panels have historically achieved some of the highest observed efficiencies however, due to the monocrystalline production process, the panels are only suitable over small areas as growing larger crystals has proven a complex and expensive procedure. It was quickly realised that the practicality of these solar panels was uncertain as they failed to maintain high efficiencies at temperatures exceeding 25 °C, substantially hindering their operating potential.[18] In order to combat these problems polycrystalline silicon solar cells composed of multiple interlocking crystals were introduced but were not capable of producing efficiencies as high as their monocrystalline counterparts. The reduce efficiencies were directly related to the polycrystalline nature of the solar cells, which possess multiple domain boundaries thus encouraging recombination of charge carrier and decreasing the ability for current to flow.[11] Despite their drawbacks, 80% of solar panels in use today are of the first-generation type, and are commonly incorporated into the exterior of buildings.[18]

The second-generation type also incorporated silicon, but conversely in the amorphous form with a layered wafer-type architecture. The production process involves depositing silicon thin films on to a glass or metal substrate, which is comparatively less time and cost effective than the respective crystalline solar cells. These solar cells did not match the efficiencies of first generation cells despite attempts to individually dope layers and facilitate absorption of a broader range of wavelengths. The failure of these layered solar cells resulted in small-scale usage, with main implementation in small handheld devices. However, the layered thin film architecture of the cell was further developed and used in the design of third generation devices.

Thus, silicon solar cells do not fulfil the high efficiency, low cost specification required for a successful commercial solar cells on a large scale. Despite this, development in the field of solar energy has continued and more recently, research has departed from the conventional silicon solar cell prototype and moved towards thin-film photovoltaic powered systems. These third generation solar cells offer low-cost manufacture coupled with competitive efficiencies that have the potential to surpass the Shockley-Queisser Limit in the near future. The most notable third generation advancements include tandem solar devices and perovskites photovoltaics. Third generation solar cells commonly incorporate naturally abundant organic

components and can be manufactured via solution synthesis at ambient temperatures. If development into this branch of photovoltaic power continues to progress then third generation solar cells are likely to replace silicon based devices in upcoming years.

1.4. Third Generation Photovoltaic Solar Energy

Third generation photovoltaic solar power is emerging as one of the most innovative fields of science in the 21st century due to the impressive properties presented by the solar cells and drive by governments around the world to tackle global warming. Third generation solar power encompasses four main variations; dye sensitised solar cells, multi-junction cells, hybrid approaches and solid-state systems. Unlike the previous generations, third generation cells often integrate both organic macromolecules and inorganic nanoparticles. These mixed molecular systems have become a focal point of research in the solar sector, as demonstrated by extensive studies into perovskite photovoltaics and hybrid polymers.

Unlike silicon solar cells, power generation in third generation solar photovoltaics is not directly through a p-n junction, but through different mechanisms of optically excited states. These solar devices are characteristically produced as thin films, similar to second generation cells, rather than a conventional panel. The thin films are in the region of a few hundred nanometres thick and can be manufactured via inexpensive solution based syntheses. They provide the added functional merits of transparency and flexibility.[18][16]

The organic constituents which make up the solid-state solar cells allow for manipulation of the properties of the cell, which is not possible in respective inorganic based devices. Through alteration of the structure of the organic molecules it is possible to tune physical aspects of the cell, for example the band gap and consequently the efficiency. The ability to interchange organic compounds, in order to produce an optimum solar cell with tailored properties gives organic containing devices a huge advantage over traditional inorganic solar cells. Hybrid organic-inorganic perovskites have made use of this technique, and through a combination of both organic and inorganic elements the solar cells have achieved impressive efficiencies of over 22%, whilst also maintaining the impressive functional properties of thin films such as transparency and high mechanical flexibility.[19]

1.4.1. Dye Sensitised Photovoltaics

Dye sensitised solar cells (DSSC) established the fundamentals upon which many of the more successful organic containing solid-state photovoltaics seen in modern solar devices are based. Although the benefits of sensitisation were realised early in the 1960s, they were not developed and integrated successfully into solar technology until 1991 by Gratzel. [20] The devices have since declared PCEs of up to 12% .[21]

Gratzel cells have proved to be the most successful DSSCs and are constructed as a large surface area, thin-film photochemical solar cell with a layer of mesoporous TiO_2 film sensitised using a molecular dye. The TiO_2 layer acts as both an electrode and a medium between the transparent conductive oxide and the hole transporting material.[22][23] The hole transporting material sits in the pores of the TiO_2 film thus inducing a heterojunction and additionally facilitating the electron hopping mechanisms in the cell.[23] The TiO_2 molecules additionally act as a semiconducting layer, yet in dye-sensitised cells the semiconductor component is used primarily for the transportation of carriers, rather than the generation of such carriers. DSSCs differ from conventional solar cells that operate via a p-n junction, as the functions of light absorption and charge carrier transport are not carried out simultaneously by the semiconducting component.[22][23] The PCEs of such cells are rely primarily on the dye sensitizer. TiO_2 semiconductors sensitised with ruthenium are responsible for the highest observed efficiencies.

In an attempt to replicate the remarkable combination of both high efficiencies and impressive functional properties seen in thin film DSSCs, solid-state sensitised perovskite cells were quickly introduced by Miyasaka.[22] The basis of the cell utilised perovskites as light absorbers, which can function without a semiconducting mesoporous layer or hole transporting material. Maximum efficiencies for perovskite solar cells were elevated 10% above those seen in Gratzel DSSCs.[23] The perovskite solar cells have repeatedly measured efficiencies that are comparable to CdTe thin film systems, and easily exceed those seen for other organic or dye-sensitised solar devices.[21-23]

1.5. Photovoltaic Perovskites

Perovskites, which were named after the mineralogist Lev Perovski, were initially discovered as the mineral $CaTiO_3$. Perovskites were generally accepted as metal oxides of the ABO_3 structure that displayed highly desirable physical attributes including ferroelectricity and magnetism. Most commonly, perovskites were thought of as purely inorganic compounds. The term *perovskite* now refers to a broader variation of crystals, all associated with the ABX_3 type structure, as illustrated in Figure 5, and incorporates hybrid structures containing organic constituents.[19]

The perovskite prototype was considered to be an ideal cubic involving a B cation with 6 fold coordination surrounded by a octahedron of O anions and a A cation with cubo-octahedral coordination.[19][21] On investigation into the ABO_3 class of crystals, it was discovered that despite displaying ferroelectric and piezoelectric properties many compositions, with limited exceptions such as $LiNbO_3$ and $PbTiO_3$, failed to exhibit good semiconducting properties.[21][23] In 2006 Miyasaka incorporated organometallic halide perovskite as an alternative dye sensitiser into DSSCs, using $MAPbBr_3$ and an I^-/I_3^- electrolyte.[23] The initial cell achieved PCEs of 2.19% but efficiencies of perovskite solar cells were elevated to 10-11% by 2012, prompting more intensive research into the class of solid-state solar cells.[19] It was discovered that this analogous class of crystals, whereby the oxygen anion was replaced with a halide, allowed for elevation of the semiconducting properties required for photovoltaic applications.

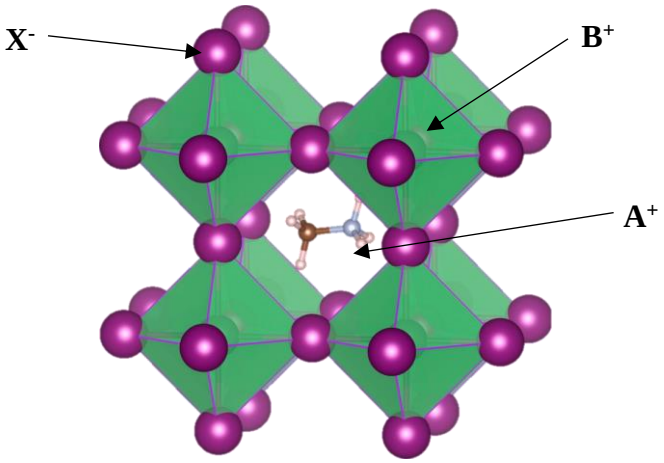

Figure 5. Typical structure of a ABX_3 perovskite crystal structure, with cubo-octahedral A site and PbI_6 octahedral framework. Where A = MA, B = Pb and X= I. [23]

1.5.1. Methyl Ammonium Lead Iodide

$MAPbI_3$ is classified as a organometallic perovskite material, and is one of the most extensively studied within the perovskite class, demonstrating the structure outlined in Figure 5. $MAPbI_3$ belongs to the family of hybrid organic-inorganic perovskites with a three dimensional ABX_3 structural framework, where A is an organic cation such as ammonium or inorganic cation such as caesium, B is a transition metal cation and X is a halide anion. The organic cation methyl ammonium, denoted as MA^+, is held in vacancies within a lead-halide framework of corner sharing PbI_6 octahedra.[19-22] The cubo-octahedral A sites are exceptionally large in order to facilitate the complex organic cations, and have 12 nearest iodide anion neighbours.[20] In usual circumstances the A and B cations would possess a divalent and trivalent charge respectively, however due to the nature of the neighbouring halogen atoms and the inherently large A site, the ions are forced to into A^{1+} and B^{2+} charge states.[19]

Introduction of lead halides in order to harvest solar cells with superior stability and photovoltaic performance was initially seen in dye-sensitised cells, but the cells lacked the desired stability due to degradation in the liquid electrolyte.[22] Subsequent incorporation of the hybrid material as a light absorbing layer has far exceeded expectations with efficiencies in excess of 23.3% and a band gap of 1.5 eV being observed. [24] It was deduced that the inherent high absorption co-efficient, long carrier lifetimes and low charge-carrier recombination allowed enhanced performance of the $MAPbI_3$ solar cells. [24]

Not only have the hybrid perovskite solar cells displayed competitive efficiencies within their class, but they also boast ease of fabrication via solution synthesis and functional advantages such as the ability to produce flexible thin-films. [19] It is the impressive PCEs and functional capabilities exhibited by the $MAPbI_3$ perovskite, coupled with the simplistic and relatively low-cost manufacture which has placed the cells at the forefront of solar cells developments.

1.5.2. $MAPbI_3$ Polymorphism

The generic perovskite structure has a cubic arrangement, however $MAPbI_3$ and its respective halide derivatives, such as $MAPbBr_3$ and $MAPbCl_3$, display many distinct morphologies. The $MAPbI_3$ structure undergoes a characteristic cubic-tetragonal-orthorhombic phase transition

which is dependent upon temperature and pressure. It is widely accepted that at ambient temperatures $MAPbI_3$ is present in the tetragonal crystal phase with corresponding *I4/m* or *I4/mcm* symmetry and unit cell parameters as follows; $a = b = 8.8756$ Å, $c = 12.6517$ Å and $\alpha = \beta = \gamma = 90°$.[25] Structural transitions are induced by an adjustment of these parameters. When the structure is subject to higher temperatures, $T > 327.4\ K$, a transition is observed resulting in a cubic crystal phase belonging to the $Pm\bar{3}m$ symmetry space group .[25] Similarly, if the temperature is significantly decreased, $T < 162.2\ K$, then a transition from the tetragonal to the orthorhombic phase with *Pnma* symmetry occurs. These transitions are aided by the dynamics of the $MAPbI_3$ crystal, specifically the rotation of the MA^+ cation and tilting of the PbX_6 octahedra. The transitions are linked to small coherent displacements of the halide ions which lead to alteration of the Pb – I – Pb angles as demonstrated in Figure 6. With temperature reduction, the angle of the Pb – I – Pb bond transitions from $\theta_{ab} = \theta_c = 180°$ (cubic phase) to $\theta_{ab} => 180°,\ \theta_c = 180°$ (tetragonal phase) to $\theta_{ab} = \theta_c => 180°$ (orthorhombic phase).[26]

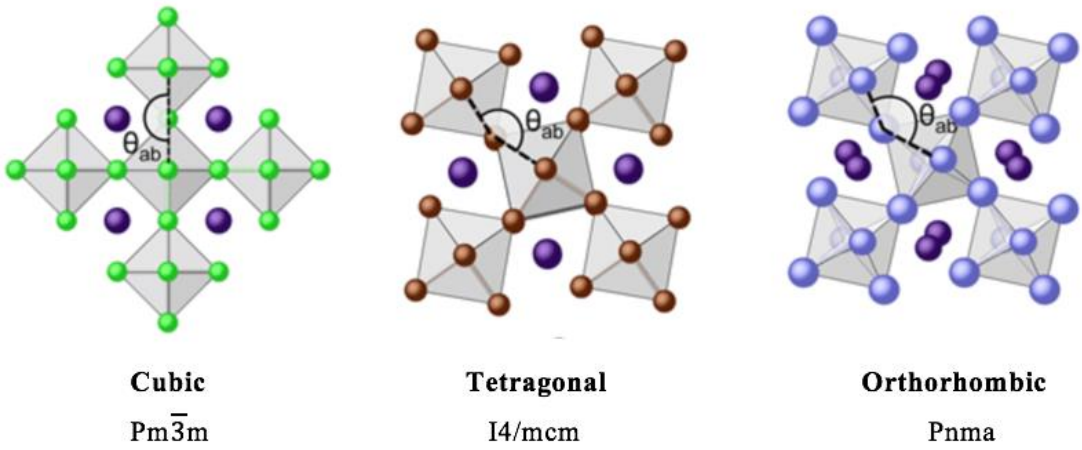

Figure 6. The three common cubic, tetragonal and orthorhombic polymorphs of $MAPbI_3$ with variation in the Pb – I – Pb bond angles when subject to thermal conditions.[26]

The Goldschmidt Tolerance Factor (*t*) is a broadly acknowledged perovskite stability and distortion indicator, which predicts stable perovskite structures using the following equation where r_A, r_B and r_o denote the radius of the A site, B site and X site ions respectively; [26]

$$t = \frac{r_A + r_O}{\sqrt{2}(r_B + r_O)}$$

A Goldschmidt tolerance factor of 1 indicates a perfectly cubic perovskite with the highest degree of symmetry. The perovskite family tend to range between 0.80 – 0.95 on the Goldschmidt scale with $FASnCl_4$ at ~0.94 $FAPbCl_3$ at ~0.91 and $MAPbCl_3$ at ~0.85.[26] $MAPbI_3$ measures slightly lower than it's analogous organochloride perovskite at ~0.83.[26]

The cubic form of the $MAPbI_3$ perovskite is inherently prone to structural instability and will tend to transform to the lower symmetry tetragonal or orthorhombic phase unless T > 327.4 K. [27] Synthesis of a cubic phase has been observed at room temperature, although under enormous mechanical pressure in the range of P > 0.4 GPa, which artificially modifies the tolerance factor closer towards the ideal t=1.[24]

1.5.3. Octahedral tilting

Octahedral tilting is a common phenomenon seen in most perovskites. The bond angles and lattice parameters of the crystal structure vary between the $MAPbI_3$ phases.[25] For example, if we consider the transition from the cubic phase to the tetragonal phase induced by decreasing temperatures, the structure is reduced to a lower symmetry, by distortion of the octahedral PbI_6 cages, therefore adjusting the Pb – I – Pb bond angles.[25] [28][29] The $MAPbI_3$ distortions, and more fundamentally the magnitude of the octahedral tilt, has been shown to be inherently linked to the electronic band structure of the material, and the absorption properties.

The octahedral tilt, outlined in Figure 7, often appears in the inorganic perovskites and is linked to the steric effects of the structure. It can be loosely quantified using the Goldschmidt Tolerance Factor. When the ionic radii are not ideally matched, the octahedral cages are driven to distort to a lower energy symmetry in order to better satisfy their environment.[31] The rigid tilting can be denoted by Glazers notation, whereby the ideal cubic phase ($a^0b^0c^0$) distorts on

decreasing temperature towards the tetragonal phase ($a^0b^0c^-$), possessing one out of phase rotation of the anion cages.[1] The low temperature orthorhombic phase ($a\text{-}b^+c^-$) exhibits both in-phase and out-of-phase rotations, and possess the lowest symmetry.[31] This phase is referred to as the ground state, with the highest degree of tilt to best satisfy the mis-match in ionic size. The degree of octahedral tilt can be quantified by calculating the difference in the dihedral angle of the I – Pb – Pb – I bond as displayed in Figure 6.[32][31]

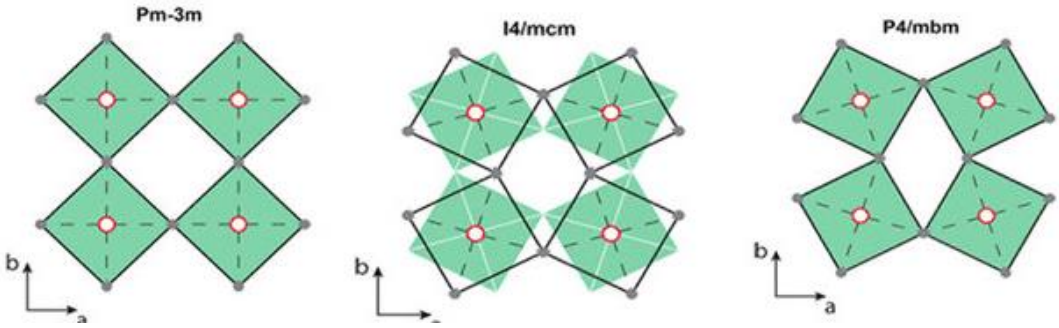

Figure 7. Schematic of the increasing degree of octahedral tilt present in the cubic, tetragonal and orthorhombic phases respectively, resulting in Pb-I-Pb angles of $\theta_{ab} = \theta_c = 180°$ (cubic phase), $\theta_{ab} => 180°$, $\theta_c = 180°$ (tetragonal phase) to $\theta_{ab} = \theta_c => 180°$ (orthorhombic phase).[26] [30]

Both experimental and theoretical studies have successfully shown that the degree of octahedral tilt can be tuned to increase the optical band gap of the perovskite material. Structural distortions such as the tilting of the octahedral are also associated with the long carrier diffusion lengths and higher carrier mobility, which are essential in minimising recombination oof free charge carriers and hence achieving superior PCEs.

1.5.4. Dynamics of the MA^+ Cation

Phase transitions are often observed in perovskites, yet the transitions of $MAPbI_3$ are unique as the order-disorder dynamics of the highly anisotropic methyl ammonium cation contribute greatly to the phase transitions.[30] It has been seen that as the structure of the perovskite deviates away from the cubic state, the cation displacement increases.[30] It has also been

observed via neutron diffraction that the low temperature orthorhombic phase exhibits fully ordered methyl ammonium cations whilst the cubic and tetragonal phases display varying levels of disorder.[30] Whilst it has been difficult to establish structure-property relationships of the $MAPbI_3$ crystal, it has been found via quasielastic neutron scattering that the rotations of the methyl ammonium cation, alongside tilting of the PbI_3 host lattice, are related to the dielectric properties. Research in the field has consistently recognised that the motion of the organic cation and the inorganic framework are interlinked.[30]

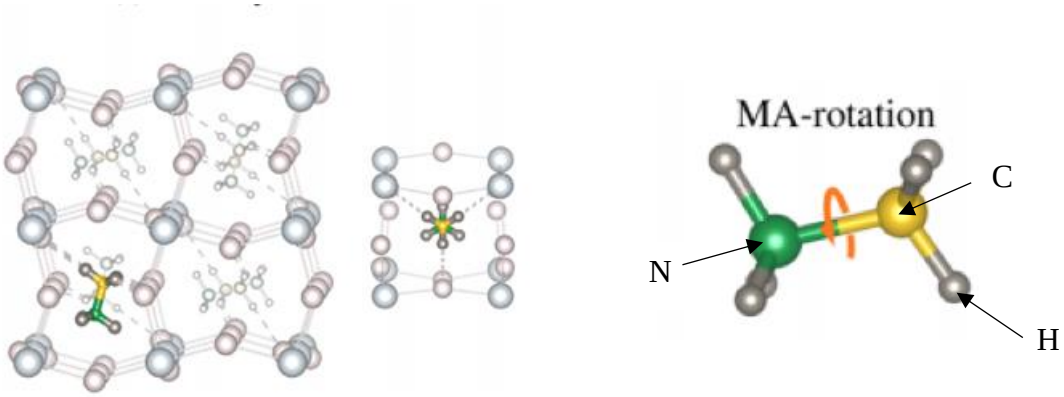

Figure 8. Model of the $MAPbI_3$ structure with dynamic rotation of the MA^+ cation ($CH_3NH_3^+$) which is able to dynamically disorder and rotate in the central cavity, performing rotations around the C-N bond as well as reorientation of the C-N bond itself.[[33]

The disordering of methyl ammonium cations becomes particularly evident in the cubic phase when the octahedral units adopt approximately 180° angles and the dynamic methyl ammonium cation which occupies a central cavity becomes disordered.[34] In fact, it has been shown by ^2H NMR that in the cubic phase the methyl ammonium cation is able to dynamically disorder and rotate in the central cavity, performing on-axis rotations around the C-N bond with a high degree of thermal and positional disorder as well as reorientation of the C-N bond itself.[34] In the cubic phase the cation displays four-fold symmetry around the C-N C_4 axis and additional three-fold symmetry around the C-N C_3 axis.[35] This is in agreement with literature that states that in the instance that $MAPbI_3$ adopts the cubic phase the methyl ammonium cation must become disordered to satisfy the reduction in symmetry from the C_{3v} group to the lower symmetry group O_h.[36]

On cooling, the rotational degrees of freedom of the cation becoming increasingly restricted. For example, in the low temperature orthorhombic phase the dynamics of the methyl ammonium cation are inhibited significantly, with the cation becoming fixed and rotation limited to the C-N bond along the C_3 axis, as outlined in Figure 9.[35]

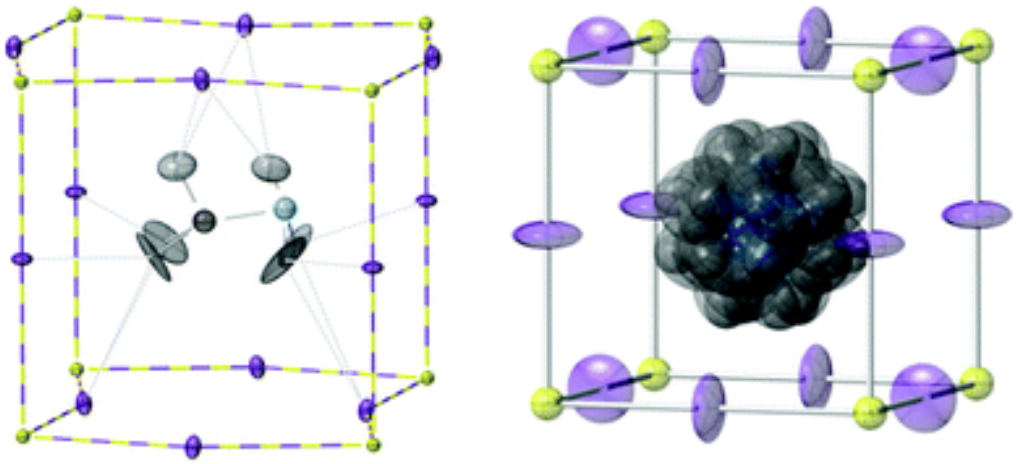

Figure 9. High orientational disorder displayed by the methyl ammonium cation in the cubic phase (right) compared to the tetragonal phase with 4 fold orientation around the c axis (left) in $MAPbI_3$.[34]

The dynamics, orientation and ordering of the methyl ammonium cation play a crucial role in the light harvesting functionality of the cell. The A site MA^+ cation contributes to features such as the low binding energy and high charge mobility of the solar cells, which in turn effect the band structure and absorption coefficient. In spite of their importance in the photovoltaic mechanism, the dynamics of the MA^+ cation are still not fully understood due to their complexity, but have been associated with ion mobility within the structure.

1.5.5. Photovoltaic Mechanism

There are few materials which have gained leverage so rapidly in the photovoltaic field as trihalide perovskites. The pivotal reasons underlying such interest is their high efficiency, low cost production and tuneable electronic properties. Their high efficiencies have been correlated with relatively long exciton lifetimes and large diffusion lengths.[37] Despite such emphasis being placed on the optoelectronic features of the cell, the photovoltaic mechanism from which they arise lacks sufficient understanding. It is the complex morphologies and dynamic nature

of the cell constituents which is responsible for the lack of clarity of the cell's light harvesting mechanism.

Although a definitive process has not yet been established it is thought that the cells photovoltaic effect is underpinned by ion migration of the possible ionic species (I^-, MA^+ and Pb^{2+}), although I^- are understood to govern this process. Theoretical activation energy ranges for ion migration have been calculated as 0.08-0.58 eV, 0.46-1.12 eV and 0.80-2.31 eV for the I^-, MA^+, and Pb^{2+} ions respectively.[38] The activation energy of the I^- anion is significant lower than that of MA^+, and Pb^{2+}, therefore it is likely that I^- are the mobile ions facilitating the photovoltaic mechanism within the $MAPbI_3$ structure.

It has been suggested that iodide anions migrate through interstitial I_2 positions within the PbI_6 cages in $MAPbI_3$, facilitated by the rearrangement of methyl ammonium cations.[39] The mechanism is consistent with electronic structure calculations which deduce that I^- vacancies are present and participate in ion transport mechanisms via interstitial migration.[40] The anomalous photovoltaic effect functions via the migration of MA^+ and I^- ions that create both MA^+ rich, n-type regions and I^- rich p-type regions, in turn establishing internal p-n junctions. These p-n junctions aid the separation of electron-hole pairs within the structure. The ion migration mechanism leads to a p-n/p-i-n type structure with a switchable photovoltaic effect.[38]

Structures which have many and large available interstitial sites are able to facilitate faster ion migration. Likewise, smaller jumping distance will promote ion migration. In $MAPbI_3$ the I^- ions at the edge of the octahera have a reduced distance (4.46 Å) with the nearest I^- vacancy compared with MA^+ and Pb^{2+}.[38] Haruyama et al summarised that I^- ions are more readily mobile compared with MA^+ ions through calculation of activation energies, 0.33 eV and 0.55 eV respectively for I^- and MA^+ ions.[38] Furthermore, ion migration of the halide ion in analogous structures such as CsPbI3 has been proven through Tubant's method.[38] Therefore it is reasonable to assume I^- is the dominant migrating species.

It has also been proposed, via bond distance calculations, that the possible formation of a redox couple yielding neutral I_2 molecules could act as an electron-hole pair; $2I^- \rightarrow I_2 + 2e^-$.[39] This would suggest an intrinsic electron transport system is functioning within the perovskite layer.

1.5.6. Internal Ionic Transport

Ionic transport is an aspect of the $MAPbI_3$ structure which also lacks depth of understanding. It is associated with many anomalous aspects displayed by the $MAPbI_3$ cell, such as the current-voltage hysteresis and switchable photovoltaic effect, as well as the photovoltaic mechanism.[40] Research has alluded to the presence of multiple Schottky defects within the structure which are believed to be related to the intrinsic ionic transport of the cell. Schottky defects are defined as intrinsic defects which arise as a consequence of vacancies in the crystal lattice, the vacancies exist as a pair formed of both an anion and cation void.[12] The thermal instability of the perovskites brings about a tendency of defect formation, particularly at grain boundaries.[40] Interstitial vacancies have an associated risk of charge trapping, however it has been shown that in the $MAPbI_3$ structure the interstitial sites are shallow acceptors thus are not critically detrimental to the efficiency.[41] Further investigation into the ionic transport of the cell is required in order to fully comprehend the photovoltaic effect.

1.6. Chemical Manipulation

Modifications to the $MAPbI_3$ structure through a variety of chemical manipulation techniques such as annealing, quenching and substitution of the A and B sites have been seen in numerous studies which results that prove promising for the future of the solar cells. Manipulation of the chemical properties of a material is performed through manipulation of its structure. Engineering of the synthetic method is often utilised in chemistry to design favourable properties or optimise properties already possessed by a chemical compound. The $MAPbI_3$ crystal is an excellent example of a structure which can readily be manipulated through various means, including simple anion/cation substitution, doping agents and post synthesis annealing processes.

Due to the solution based processing of the materials it is easy to interchange the cation and anion sites. Research has frequently seen the production of $MAPbBr_3$ and $MAPbCl_3$ crystals, or alternatively mixed halide perovskites. What might appear as minor compositional changes can have significant effects on chemical properties for instance the band gap or stability. This is seen on comparison of the $MAPbI_3$ and $MAPbBr_3$ structures, the latter of which has a decreased unit cell and increased stability consistent with shorter Pb – X – Pb bonds.[42] A

study conducted by Noh et al has shown that substitution with bromide ions in the X site is also able to tune to bandgap range of the material from 1.5 eV and 2.7 eV. [43] Likewise, replacing the iodide anion site with chloride anions results in narrowing of the bandgap and superior photovoltaic properties.[44] Similarly, substitution of the A cation in $MAPbI_3$ site is also reported, where caesium or rubidium has proven to enhance stability due to an entropic stabilisation related to the decreased cation size. Both $FAPbI_3$ and $CsPbI_3$ have displayed better thermal stability that $MAPbI_3$. [43]

Material design of the photovoltaic perovskites can go beyond the initial synthetic stages and take place post synthesis, for instance annealing treatments of the $MAPbX_3$ crystals. Annealing was initially implemented to increase the crystallinity of the phase and remove excess solvent however it was quickly realised that it could be used to make informed modifications to the structure. The physical and chemical properties of the perovskite are highly sensitive to duration, temperature and conditions of the annealing environment.[45] Generally, optimal annealing conditions for $MAPbX_3$ perovskites generally range between 10 – 70 minutes and in the range of 80-160 °C.[44]

On exposure to different chemical or thermal environments, it has been seen that structural alterations can take place. In a study conducted by Zohar et al, a $MAPbI_3$ thin film was doped with I_2 vapour post synthesis. The results indicated that the film was ten times more electronically conductive, with a small red shift in photoluminescence. Manipulation of the perovskites by non-chemical related means such as high pressure using a diamond-anvil cell has also been reported.[24]

1.7. Intrinsic Instability of $MAPbI_3$

While $MAPbI_3$ and its halide derivatives offer a high efficiency, low cost thin film solar cell which meets many of the specifications for a viable solar device there are still factors inhibiting its success. If the solar cells are to become a viable source for renewable energy the poor long-term stability and degradation issues of the perovskite must first be addressed. The stability of a solar device is synonymous with its ability to withstand external factors.

Research has shown that in fact the perovskite structure is highly susceptible to degradation on exposure to factors such as air, moisture, UV light and thermal energy.[46] The perovskites are known to degrade on exposure to water vapour at ambient temperature or thermal stress above 85 °C, into PbI_2 and a MAI by-product, the former of which hinders the cells photovoltaic effect. [47][46] Such degradation is attributed to the strength of the Pb – I – Pb bonds and thus the stability can be quantified by the breaking of these bonds.

The internal factors such as the intrinsic thermal instability of the $MAPbI_3$ structure and the hygroscopic nature of the MA^+ cation further contribute to the instability of the cell. The thermal tolerance of the cell is crucial to its success as solar cells are required to function over the temperature range of -40 °C to 85 °C if they are to be implemented on an international scale.[48] It has been shown that increased thermal stabilities can be achieved on replacing the MA^+ cation with a FA^+ cation or an inorganic Cs cation.[48] The resulting perovskites have increased thermal stability and can withstand an additional 15 °C before decomposition when compared with $MAPbI_3$.[48]

Mitigations such as encapsulation of the solar cell and use of additives have been suggested yet this often compromises the efficiency of the cell and does not directly solve the stability problem. Thus far the longest lifetimes of a photovoltaic solar cell have been reported as one year, which is radically shorter than the average 25 year lifetime of a conventional silicon solar cell.[49] This places prominence on the need for rapid development of the stability of perovskite based cells.

1.8. Toxicity Concerns

The use of the toxic element Pb which occupies the B cation site is an additional feature which must be tackled if the perovskite solar cells are to be considered for commercialisation. Lead is toxic both on exposure to humans and to the environment on disposal of the solar panels. Hence Pb is essentially impractical as the B site cation. Tin or bismuth offer feasible alternatives and research into these elements is ongoing, yet achieving power conversion efficiencies as high as lead-incorporating devices may prove a challenge. Tin offers the added advantage that, unlike $MAPbI_3$, it adopts a high symmetry pseudocubic structure at room

temperature and has a decreased band gap of 1.3 eV.[50] However stability still remains a concern for the tin-halide perovskites as tin is susceptible to rapid oxidation of Sn(II) to Sn(IV).[50][51]

Bismuth is able to provide an alternative that is both stable at ambient temperatures and non-toxic. Yet simply interchanging the lead site with bismuth does not result in a perovskite structure.[52] Research for viable alternatives for the B site cation is ongoing and advancements are moving towards lead-free PV solar cells. Ultimately, if the toxicity and stability issues can simultaneously be solved within one fully functioning solar cell without compromising the efficiencies as exhibited by $MAPbI_3$ then a feasible PV solar cell will be attained.

1.9. Synthetic Methods

The synthesis of $MAPbI_3$ is varied throughout research depending on the desired form of the perovskite sample, ranging from thin films to nanoparticles. There is a strong composition-structure relationship of the $MAPbI_3$ crystal. Therefore, the structural and physical properties are heavily influenced by the synthetic method. There are four principal synthetic methods that are ubiquitous in $MAPbI_3$ research; the spin coating method, the precipitation method, the solid-state method and vapour decomposition.

For production of thin films a spin coating method must be implemented which can consist of either a one or two step process. The one-step method spin coats a mixture of PbI_2 and MA dissolved in an organic solvent onto a substrate, or alternatively the two-step method coats the PbI_2 individually onto the substrate which is afterward immersed in a MA solution.[53] The spin-coating method often results in a inhomogeneous polycrystalline coating therefore an annealing process is implemented following the spin coating process to ensure q high degree of crystallinity.[54] Preparation of thin films by vapour deposition is another popular technique which offers increased uniformity compared with spin coating but at the expense of high power conversion efficiencies. It involves exposing the substrate to vapour produced via sublimation of PbI_2 and MAI powders.[53]

Solution processing is an alternative technique often used to synthesis nanoparticles or powdered samples. It involves precipitation of the perovskite crystal from a precursor solution of PbI_2 and MAI in excess solvent. The solution based method can result in highly

monodisperse samples or the production of multiple morphologies.[54] The method benefits from its simplicity and ability to be carried out at relatively low temperatures, making it an inexpensive and rapid synthesis, favourable for bulk manufacture. Synthesis of mixed-halide hybrid perovskites, where the X site is occupied by more than one halide anion, has been achieved via simple solid-state reactions where two solution processed powders are thoroughly ground together.

Solid state synthesis provides a solvent free, mechanochemical method. The process often utilises ball milling of solid precursor materials in batch, however may be carried out manually using a simple pestle and mortar for small-scale experimental purposes. The solid state method allows superior control over the stoichiometry compared with traditional solution based synthesis. The quick and simple tuning of the stoichiometry of the sample and lack of solvent impurities is advantageous, however the solid state method is not favourable for Pb containing trihalide perovskites.

Chapter 2: Characterisation Techniques & Technical Theory

2.1. X-ray Diffraction Theory

X-rays are a form of transverse high energy electromagnetic radiation, that propagate in a wave.[56] One method of generation of x-rays relies on the irradiation of matter by highly charged particles such as electrons. In standard laboratories a metal would be heated in order to overcome a threshold thus emitting electrons which can been accelerated by an electric field to the desired metal target, most frequently copper or molybdenum, which acts as the anode. This is known as the cathode x-ray tube method. During this process 99% of the energy of the beam is lost as heat energy whilst the remaining 1% is lost by collision of the accelerated electrons, this is referred to as *white radiation*.[57] The shortest wavelength that may be obtained is limited by the maximum energy lost. The energy of the radiation is as defined by the following equation: [58]

$$\boldsymbol{E = eV = hc/\lambda}$$

Where *e* is the charge of the accelerated electron, *V* is the voltage of the acceleration, *h* is Plank's constant and *c* is the speed of light. It is possible to obtain longer wavelengths through a multiple collision process and for shorter wavelengths a higher accelerating current is necessary. This process is not useful for analysis techniques, however in the instance that the energy of the emitted electrons is higher than a threshold, characteristic to the metal target, then *characteristic radiation* can be generated.[58] Characteristic radiation forms discrete peaks within a spectrum which are as a consequence of an electron from the inner shells of the metal atom being ejected and subsequently replaced by an electron from an outer atomic level. By filling the vacancy, the electron from a higher orbital has lost energy, therefore an x-ray emission is generated with an energy characteristic of the energy difference between the quantised energy levels, ΔE. Transitions are governed by a set of selection rules, which have strict forbidden transitions, resulting in a few select spectra lines.

The characteristic spectrum consists of multiple radiation components, most fundamentally K_α and K_β, which relate to the orbitals involved in the transition. If the orbitals are adjacent, and hence their principle quantum numbers differ by ±1 then the radiation is referred to as alpha.[58] If the transition occurs across more than one shell, and the difference between the principle quantum number is greater than one, then the radiation is referred to as beta. The energy difference has an inverse relationship with the wavelength of the radiation emitted as outlined: [58]

$$\Delta E_\beta > \Delta E_\alpha \, then \, \lambda_\alpha > \lambda_\beta$$

This corresponds to the wavelengths for copper metal which are 1.542 Å and 1.392 Å for $K_{\lambda\alpha}$ and $K_{\lambda\beta}$ respectively. This is also true for the commonly used molybdenum. However, the majority of the K_β radiation is filtered out alongside the white radiation during the monochromatic process, leaving a single wavelength which can be directed towards the sample for the purpose of diffraction.[58]

On interaction with the sample the x-ray radiation is scattered in all directions, it is only when the radiation scatters in phase and is able to satisfy Bragg's Law that a diffraction pattern can occur. Both M. von Laue and W. L. Bragg made revolutionary discoveries in the field of x-ray analysis in 1912 of which Bragg's is taken as the most simplistic model and has become extensively used for describing x-ray diffraction.[11] Bragg's Law is arguably the most important equation in relation to diffraction and defines what is actually observed when the x-radiation reaches the crystalline sample: [11]

$$n\lambda = 2d_{hkl} \sin\theta$$

Where n is an integer that corresponds to the order of diffraction, λ is the wavelength, d represents the d-spacing and θ is the angle between the incident radiation and crystal lattice plane. Lattice planes can be envisaged as parallel planes separated by spacing defined as d_{hkl}.[59] Although it is often stated that the lattice planes are responsible for scattering of the x-ray beam this is simply a theoretical concept and it is in fact the electron clouds of the constituent atoms that produce the diffraction pattern. If Bragg's Law is satisfied by the scattering from two lattice points then constructive interference occurs resulting in the phenomena that is

diffraction. Constructive interference can occur on the condition that the pathlengths between the reflection from two consecutive planes is an integer multiple of the wavelength, λ.[11]

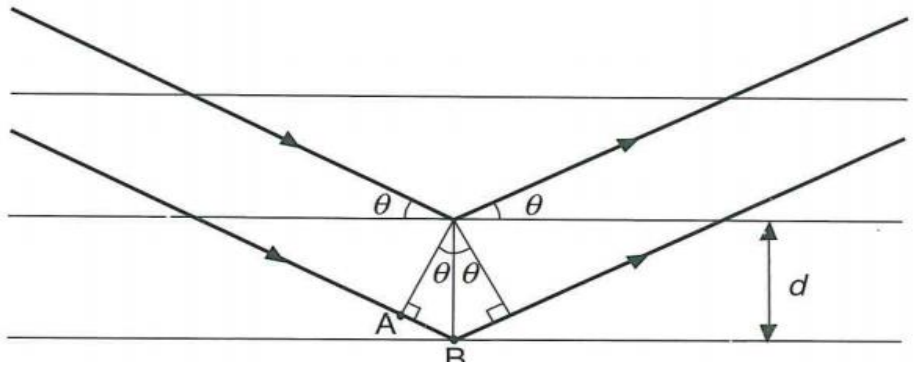

Figure 10. Schematic representation of Bragg's Law; $n\lambda = 2d_{hkl}\sin\theta$. Outlining the respective lattice planes and scattering of an incoming source.[11]

Bragg's Law concludes that diffraction is an arranged event that relies on three parameters; the wavelength, orientation of the crystal and the d-spacing. Hence if the d-spacing is defined and a specified wavelength is used, then by altering the crystal orientation and therefore the θ angle, inevitably Bragg's Law will have the opportunity to become satisfied. This is the principle upon which powder XRD is based. The XRD monochromatic mode works with a constant wavelength and fixed d spacing, the crystal is then rotated through a range of θ angles until Bragg's equation is fulfilled and a diffraction pattern is obtained which displays intensity as a function of the scattering angle, 2θ.

Synchrotron x-ray sources are proclaimed as one of the most significant developments in diffraction analysis. A synchrotron source of radiation is emitted when charged particles travelling in space are forced to change direction due to passing through a magnetic field.[72] Synchrotron facilities produce extremely high energy, short wavelength radiation which can be up to 5 orders of magnitude greater than the conventional x-ray cathode tubes.[73] Synchrotron radiation is generated in high vacuum tubes or storage rings when charged particles are accelerated to high speeds ($\sim 3 \times 10^8$ ms^{-1}) and circulate due to the field of a bending magnet. Synchrotron radiation is able to provide high intensity over a wide range of wavelengths, this ability to tune the desired ratio of wavelength and intensity have led to huge advancements in structural determination.

An alternative method of diffraction is based on is the Laue mode, which involves a static sample but varies the wavelength of the beam. Laue used a white beam and a stationary sample, as opposed to a monochromatic beam, in his initial x-ray diffraction experiments.[58] Since the crystal is static the angle θ and d_{hkl} spacing becomes constant by default. It is essentially the crystal planes which differentiate which wavelengths (λ) can diffract. In order to understand single crystal x-ray diffraction in some depth, we must refer back to the Laue model.

Two mathematical constructs which are pivotal to the foundations of x-ray diffraction are *Reciprocal Space* and the *Ewald Sphere*, these were essentially founded on the principle of the Laue equations. Laue summarised that a crystal possesses direct space, which defines the physical lattice points and can be described by vectors *a*, *b* and *c* and that the reciprocal space of the lattice is described by the reciprocal of these vectors, for example *a**, *b** and *c** which lie at the intersection of equidistant parallel planes.[60] The reciprocal lattice, also known as Fourier space, is a set of hypothetical lattice points which are the allowed terms for Fourier space. They are strictly allowed if the point is consistent with the periodicity of the crystal and, on scattering, the change in wave vector is a vector of the reciprocal lattice.[61] The Ewald Sphere is a geometrical representation of such a theory, which establishes which of the reciprocal space point may diffract. When the reciprocal lattice intersects the Ewald sphere the Laue diffraction condition is fulfilled. The consequent diffraction patterns can be recorded using photographic film or more modern electronic detectors.[62]

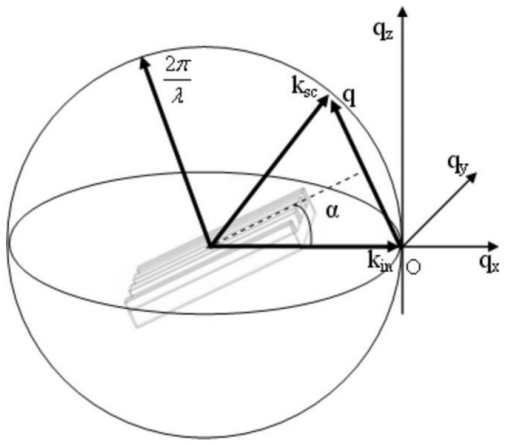

Figure 11. Illustration demonstrating Ewald's Sphere and how the it may be used in conjunction with the reciprocal space to determine the site of a diffraction spot respective to the incident beam.[63]

2.2. Rietveld Refinement Method of Powder XRD

The acquired powder and neutron diffraction data was refined using the Rietveld method which serves as a quantitative phase analysis to determine the atom positions, space group and unit cell parameters of the crystalline sample. The method was developed and publish by Rietveld in 1967 in a paper pertaining to diffraction patterns which have a characteristic set of intensity peaks at each defined 'step' which corresponds to either increments of energy (i.e. velocity in respect to TOF profiles) or scattering angle (i.e. 2θ angles in respect to PXRD profiles). The collection of individual reflections each have a corresponding peak height, peak position and breath, a peak tail which decays with distance from the peak and an integrated area which is specific to its corresponding Bragg intensity, I_{hkl}.[64] The determination method works on the basis of a least squares minimisation method between an observed and a calculated profile via multiple iterations.[64] The quantity minimised (S_y) is defined by the following equation where y_i is the observed intensity at the *i*th step and y_{ci} is the calculated intensity at the *i*th step and w_i is the negative reciprocal of y_i ; [64]

$$S_y = \sum_i w_i(y_i - y_{ci})^2$$

The method involves, but is not limited to, refining the following fundamental factors; intensity, variable lattice parameters, linear absorption coefficient, background peaks and the scale factor. It is also possible to refine isotropic and anisotropic factors and instrumental variations in order to obtain an accurate refinement as defined by a Chi-squared value of 1 (χ^2= 1). Determination of the crystal structure solely from the diffraction patterns pattern is a complex procedure hence numerous programmes and software packages have been developed over time to assist in refinement of data. In this case, the Fullprof Suite software was utilised for refinement of both the powder x-ray diffraction and neutron diffraction data in order to obtain structural information. Structural refinements of the single crystal measurements were solved using the SHELXS and SHELXL software suites.

2.3. Neutron Diffraction Theory

Neutron sources are often used as an alternative or indeed as a complimentary analytical device for x-ray diffraction. Contrary to x-rays, neutrons probe the specific positions of the nuclei within the sample rather than the electronic clouds.[64] It is known that neutrons travel slower than respective x-rays and are inherently charge neutral hence they interact relatively weakly with matter.[11] Despite the weak interaction of neutrons, they are in fact able to penetrate deeply into the target and due to the absence of charge there is no Coulomb barrier on incoming to the nuclei.[66] The de Broglie equation relates the momentum *p* of a neutron to the wavelength of the corresponding electromagnetic wave:

$$\lambda = \frac{h}{p} = \frac{h}{mv} = \frac{h}{(2m\xi)^{\frac{1}{2}}}$$

Where *m* is the mass and ξ the energy of the neutron. Neutron beams are produced by either a fission reaction within a nuclear reactor or via a spallation process involving a high energy beam of protons that in turn radiate neutrons.[67] Neutron sources formed as a by-product of a nuclear reaction result in a continuous beam with time, whereas those produced via spallation give out pulses of radiation, coupled to clusters of protons that irradiate the target.[68] As with most electromagnetic radiation, the neutrons produced will comprise a broad distribution of energies.[62] Passing the neutrons through a moderator will thermalize their energy, where their resulting energy is equal to $3K_BT/2$.[68] If the moderator is set to ambient temperature the neutrons that are output have a λ in the region of 1.5 Å, which is comparable to interatomic spacing and hence ideal for diffraction.[68]

It is possible to generate monochromatic thermal neutron beams, however in respect to a pulsing neutron source the energies are often too high for useful applications, hence they are decelerated to remove some magnitude of the kinetic energy.[62] The neutron source is directed towards the sample, each neutron moves in space at a specific speed related to its velocity.[62] Incident neutrons reach the sample and are scattered by the nuclear forces within the crystal, which in this case is referred to as the scattering system. When the neutron reaches the detector, the flight time is logged. The data is recorded as intensity as a function of flight time.[62] The wavelength can be calculated using the following equation which relates the total distance travelled between the moderator and detector *L* to the flight time: [62][68]

$$\lambda = \frac{ht}{mL}$$

If we associate this to the de Broglie's principle: [62]

$$d = \frac{ht}{2m\,L \sin\theta}$$

This provides an equation which relates the time of flight to the d-spacing within a crystal, and can hence be used to assist in determination of the structure and atomic parameters of a sample.

The principal reason which makes neutron data appropriate for consolidation of x-ray data is that neutrons are able to strongly diffract even with the lightest of elements, for example hydrogen which interacts weakly with x-rays but gives sizeable neutron scattering. Moreover, due to the different scattering mechanisms of x-ray and neutron diffraction, neutrons offer other advantages such as their ability to distinguish between different elemental isotopes.[64] X-ray diffraction works on the basis of scattering electrons, and thus the scattering is proportional to the electronic density and therefore the mass of the atom. However, neutron scattering does not vary linearly with Z.[64] It must also be noted that neutrons possess a spin and a magnetic moment, so are useful in determining the electron spin arrangement and density distribution of unpaired electrons, offering insight to the magnetic properties of a material. It is when used in unison that these analytical techniques provide the most reliable data. Both neutron and x-ray diffraction were utilised within this project.

2.4. Characterisation Instruments

2.4.1. X'pert^3 PANalytical X-ray Diffractometer

Powder x-ray diffraction determines properties of the 'bulk' of a sample, giving insight to sample purity and morphologies. The technique gives an overview of a large sample and may be used to give a fingerprint spectrum.[58] The X'pert^3 PANalytical diffractometer was used to carry out powder x-ray diffraction data collection. Each of the photovoltaic perovskite samples

were scanned over a 3-hour time period, in the 2θ range of 0 to 80 degrees with a step size of 0.0084 in order to obtain a high resolution scan. The samples were first ground to a fine powder before being mounted onto a zero background Si plate. Although it is not always necessary for powder diffraction, in this case the sample is rotated in order to achieve better powder averaging. All measurements were taken in air, at room temperature.

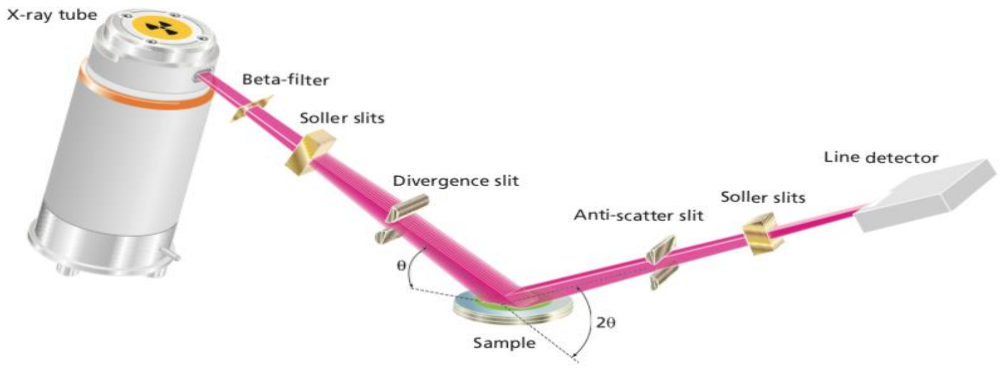

Figure 12. Diagram representing the internal process of the X'pert3 Powder X-ray Diffractometer.[69]

Within the diffractometer x-rays are generated at the cathode x-ray tube but do not reach the sample until they pass through the beta filter and various collimating slits. The x-rays are first passed through soller slits which assist in achieving higher resolution, especially at low scattering angles, following this the beam enters a divergence slit which governs the equatorial distance of the beam over the sample. After interaction with the sample the beam enters an anti-scatter slit in order to minimise background and decrease any unwanted scattering, eventually the beam arrives at the line detector, as outlined in Figure 12. The data is compressed into a 1D form.

2.4.2. Supernova Single Crystal X-ray Diffractometer

Single crystal x-ray diffraction allows for the absolute structure to be determined as the exact atomic positions can be measured, allowing for determination of bond lengths and angles. Single crystal x-ray diffraction data is collected in 3 dimensions resulting in more discrete peaks with less overlap compared with powder x-ray diffraction.

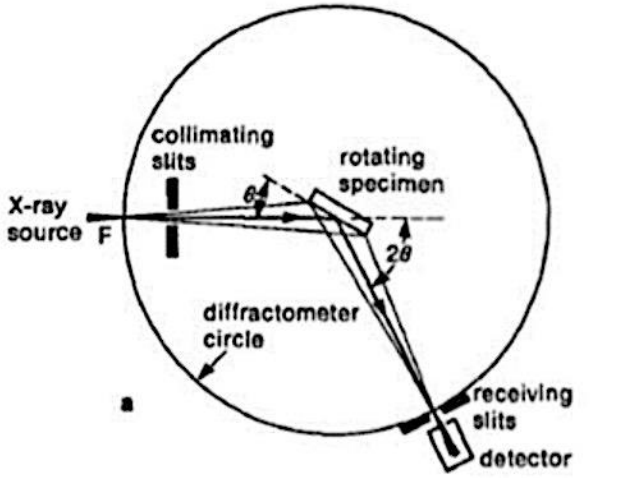

Figure 13. Fundamental concept of how a single crystal x-ray diffractometers works.[70]

All single crystals measurements were obtained using the Supernova Single Crystal Diffractometer Aglient by Oxford Diffraction. It is a dual wavelength diffractometer which is able to scan using either a copper or molybdenum K_α x-ray source. Due to the low-temperature Cyrosteam system the diffractometer has temperature control in the range of 80 to 500 Kelvin.[71] The diffractometer is comprised of two micro focused x-ray tubes, an x-ray shutter, a goniometer for orientation of the sample, and a beryllium window accompanied by a CCD detector. Also present is a video microscope in order to align the beam to the sample, and a number of collimating slits. The sample is rotated through a full 360° angle while intermittently exposed to the x-ray beam to obtain a full sphere scan. Once each individual irradiation of the sample at a specific orientation occurs, the beam goes on to reach the detector. The charge coupled device detector works on the basis of converting the x-rays, which enter through the beryllium window, to photons of light via a scintillation screen. The phonons are transported by fibre optics towards the CCD chip and stored for analysis.[71]

2.4.3. BM01 SNBL Diffractometer

High resolution diffraction using a synchrotron radiation source was carried out at the ESRF Facility using the Swiss Norwegian Beam Lines (SNBL). The BM01 beamline was used to acquire single crystal diffraction data, whilst the BM31 beamline was used for the purpose of powder diffraction data. The beamline works on similar principles to usual diffraction despite

the synchrotron source. The diffractometer makes use of an imaging plate detector to enhance the spatial resolution and a double crystal monochromator.[72]

2.4.4. Powgen Neutron Diffraction Source

Neutron diffraction data was obtained in order to consolidate the collected x-ray diffraction and provide further in site in to the structure at the atomic scale. The neutron data was collected at the Oak Ridge National Laboratory using the Powgen Neutron Diffractometer. The Powgen instrument is a third-generation diffractometer which utilises a spallation radiation source to produce time-of-flight data from a remarkable 60 m flight path. However, unlike other spallation neutron sources the geometric design allows for the scattered neutrons to be collimated in a single diffraction pattern that presents a high count rate coupled with high resolution, rather than a data set from each detector bank.[73] The third-generation construct allows the instrument to collect data over a large range of d-spacing due to the narrow bandwidth which gives rise to wider angular coverage.[73]

Chapter 3: Synthesis, Results & Discussion

3.1. Purpose of the present studies

The present studies seek to explore and evaluate a range of chemical manipulation techniques, and identify how these techniques may encourage a change in the structure of the typical $MAPbI_3$ perovskite.

3.1.1. Synthesis Overview

Methyl ammonium lead iodide was synthesised following the same methodology throughout all conducted experiments. Methodology is outlined below.

The stages of synthesis involved the initial formation of the starting material CH_3NH_3I (denoted MAI), followed by preparation of a precursor solution based on a 1:1 ratio of MAI and PbI_2. The precursor solution eventually yielded the desired $MAPbI_3$. The synthetic method was adapted from prior research in the field.[55] The reaction scheme was as follows:

$$MA + HI \rightarrow MAI$$
$$HI + PbO \rightarrow PbI_2 + H_2O$$
$$PbI_2 + MAI \rightarrow MAPbI_3$$

Once synthesised, the $MAPbI_3$ crystals were annealed in several controlled environments. Characterisation techniques including powder XRD, single crystal XRD and neutron scattering XRD were performed to achieve insights into how the structural makeup of the perovskite could be manipulated.

3.1.2. Synthesis of Prototypical $MAPbI_3$

Synthesis of methyl ammonium iodide: Equimolar amounts of hydroiodic acid 57% w/w aqueous solution (10.6 mL) and methyl amine 40% w/w aqueous solution (5.8 mL) were cooled to below 0°C whilst stirring in separate conical flasks for 1 hour. Once cooled methyl amine was added dropwise to the stirring hydroiodic acid and the resulting solution removed from the

ice bath to return to room temperature. The solution was then heated at 80 °C for 48 hours, with intermediate stirring, to produce a crystalline white solid. The crystals were washed with acetone (5-10 mL) and collected via vacuum filtration using a Buchner funnel. (Yield = 7.65 g)

Synthesis of methyl ammonium lead iodide: A precursor solution of hydroiodic acid 57% aqueous solution stabilised with 1.5% hypophosphorous acid (10 mL) and hypophosphorous acid (1.7 mL) were heated at 120°C whilst stirring for 10 minutes. Lead oxide (2.23 g) was added to the solution, which was continually stirred until the orange solid had fully dissolved, affording a yellow solution. At this point methylammonium iodide (1.35 g) was added, resulting in instantaneous formation of black crystals within the solution. Heating was discontinued for 10 minutes to promote crystallisation on the remaining dissolved solute, before returning the solution to the heating mantle for an additional 5 minutes. The resulting iridescent black crystals were collected via vacuum filtration using a Buchner flask. (Yield= 2.25 g)

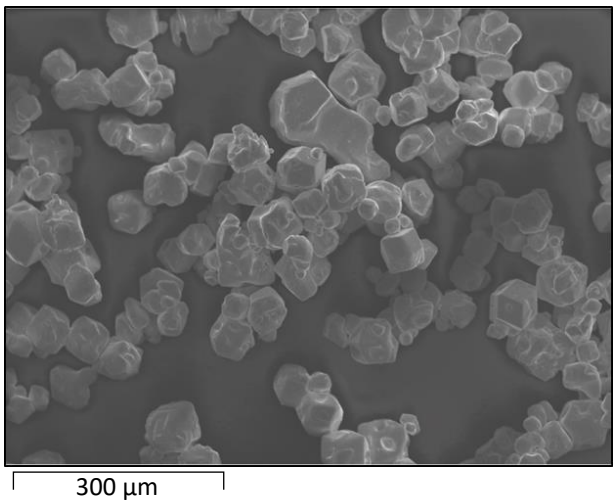

Figure 14. Scanning electron microscope (SEM) imaging was performed at room temperature of the solution synthesised $MAPbI_3$ crystals.

3.2. Prototypical $MAPbI_3$

The prototypical $MAPbI_3$ sample refers to the synthesised $MAPbI_3$, prior to any chemical manipulation techniques, including the introduction of post synthesis thermal heating. The structural properties and nature of transitions of the prototypical $MAPbI_3$ sample were

established for comparative purposes. The aim of the present study is to explore chemical manipulation techniques and the alterations that may occur in relation to the structural and chemical properties of the $MAPbI_3$ perovskite material as a result. The studies are concerned primarily with the structure of the unit cell and the tetragonal-cubic phase transitions of the $MAPbI_3$ structure.

X-ray powder diffraction data of the prototypical $MAPbI_3$ was obtained via the BM31 beamline at the ESRF facility, using $\lambda = 0.956910$. The x-ray diffraction data obtained from the prototypical $MAPbI_3$ sample was refined using the Fullprof Refinement Suite and confirmed correspondence with the commonly accepted I4/mcm tetragonal room temperature $MAPbI_3$ structure as reported in previous literature.[25] The archetype tetragonal $MAPbI_3$ lattice is primarily constructed of PbI_3 octahedral cages which exhibit out of plane distortions, corresponding to the Glazer co-ordinates $a^0b^0c^-$, alongside the organic methyl ammonium cation.

Rietveld refinement confirmed that the $MAPbI_3$ sample was in the tetragonal phase, belonging to the space group I4/m with respective lattice parameters a = b = 8.86882 Å c = 12.66637 Å and $\alpha = \beta = \gamma = 90°$. The XRD profile demonstrated the 110 reflection characteristic of the tetragonal $MAPbI_3$ compound, and the nature of the sharp peaks which make up the profile are synonymous with a highly crystalline sample produced via solution synthesis. The XRD refinement profile revealed minimal impurity peaks suggesting a high purity crystalline phase, although a peak at 12.7 2θ does indicates some form of PbI_2 impurity within the sample, often seen in solution synthesis of $MAPbI_3$.

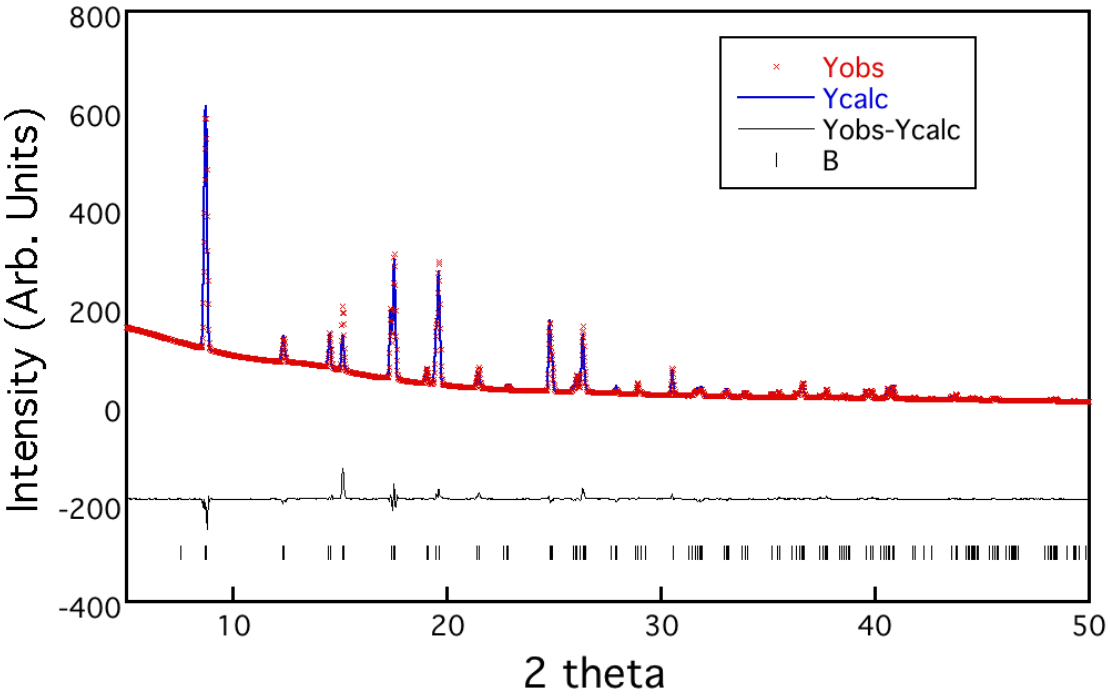

Figure 15. Powder XRD profile for Rietveld refinement of the prototypical $MAPbI_3$ sample at 290 K obtained at BM31 diffractometer. Where Yobs is the measured pattern, Ycalc is the structural model used to refine the profile, Yobs-Ycalc is the difference in the two profiles and B is the Bragg position

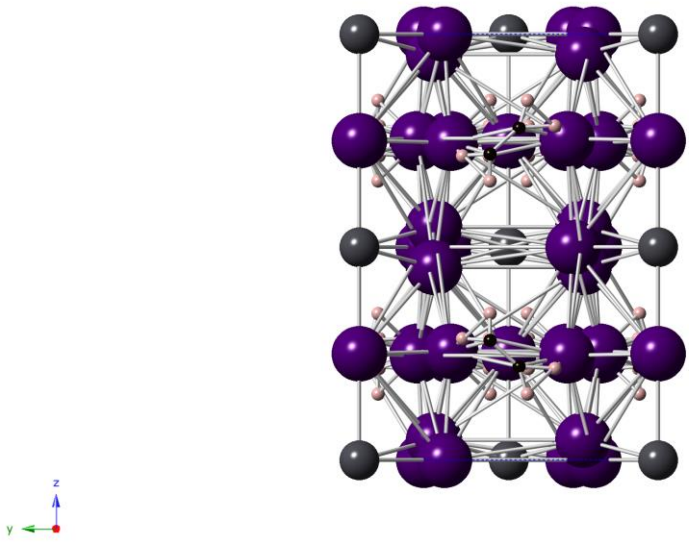

Figure 16. Unit cell model of the tetragonal prototypical $MAPbI_3$ structure derived from the powder x-ray diffraction Rietveld refinement

Atom	***x***	***y***	***z***	**Occ.**
Pb1	0.0	0.0	0.0	0.99
Pb2	0.0	0.0	0.5	0.95
I1	0.0	0.0	0.25	1.0
I2	0.21197	0.28804	0.5	1.0
N1/C1	0.55870	-0.00628	0.29257	0.349

Table 1. Atomic positions and occupancy for tetragonal prototypical $MAPbI_3$

Variable temperature x-ray powder diffraction was carried out over the temperature range 100 K – 400 K in order to induce an amorphisation that the prototypical $MAPbI_3$ is known to undergo as a function of increasing temperature. At 345 K the tetragonal structure transitioned to a small cubic unit cell with lattice parameters a = b = c = 6.30382 Å. The tetragonal-cubic transition temperature is slightly increased in the prototypical $MAPbI_3$ sample compared to the temperature reported in the literature of 327 K. However, it is acknowledged that $MAPbI_3$ shows some variation in transition temperatures depending on the synthetic route.[25] The

transition to the $Pm\bar{3}m$ cubic phase as the temperature increases is quantified by the lattice parameter ratio which is defined by the equation $c/\sqrt{2}a$.

Figure 17 demonstrates that as the temperature rises the ratio moves closer to 1, and at 330 K the ratio dramatically decreases signifying that the structural transition had begun to occur, as the *a* lattice parameter increases and the *c* lattice parameter decreases simultaneously as the crystal moves towards a more uniform structure. The experimental data shows that once the temperature exceeds 345 K the *a* and *c* lattice parameters converge and a simple cubic structure of $MAPbI_3$ is observed. This transition is associated with reduction in PbI_6 octahedral tilt and shorter Pb-I bond lengths as the cell takes the higher symmetry cubic form.

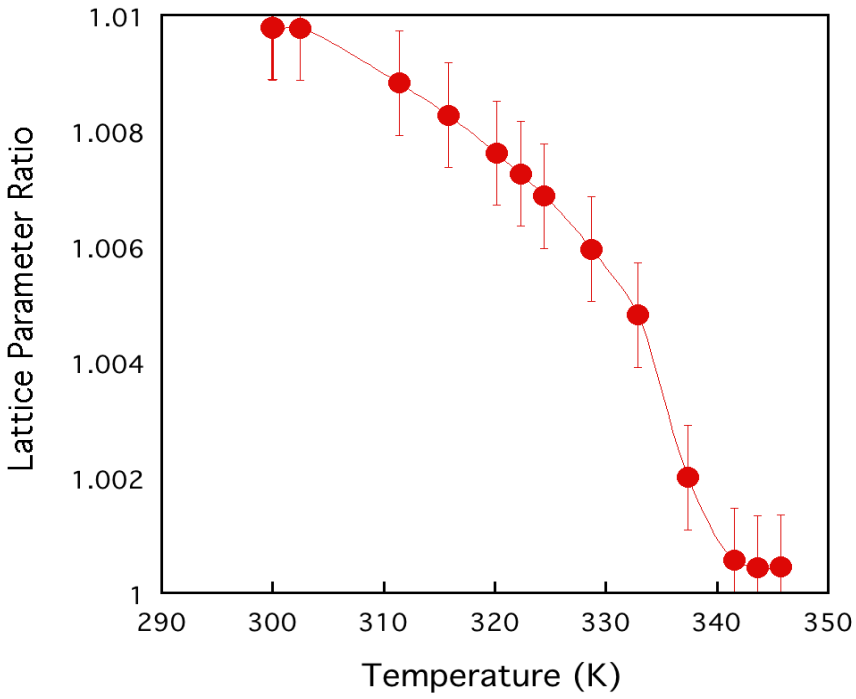

Figure 17. Plot of the $c/\sqrt{2}a$ lattice parameters as a function of temperature during the tetragonal-cubic transition of prototypical $MAPbI_3$ derived from powder XRD carried out at 290 K obtained at BM31 diffractometer.

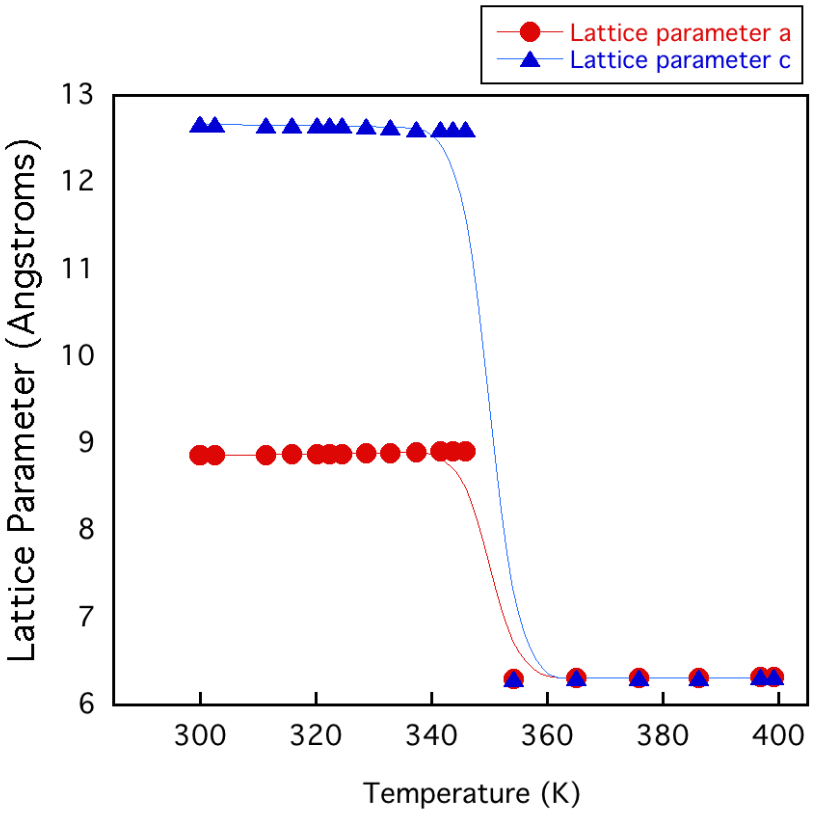

Figure 18. Lattice parameters as a function of temperature, outlining the thermally induced tetragonal-cubic transition of prototypical $MAPbI_3$ at 345 K derived from powder XRD carried out at 290 K obtained at BM31 diffractometer.

Using the results of the refined powder XRD profile obtained at 290 K on the BM31 diffractometer the Pb – I – Pb dihedral bond angles were determined. The results confirm the transition towards the higher symmetry cubic phase, quantified by the increasing bond angle. The Pb – I – Pb angle increases until 345 K where the temperature conditions satisfy the cubic phase change, at which point the bond angles become equal to 180.00° as outlined in Figure 19. The determined bond angle determined at 345 K is characteristic of the $Pm\bar{3}m$ space group, described as a zero-tilt system with $a^0b^0c^0$ Glazer co-ordinates.

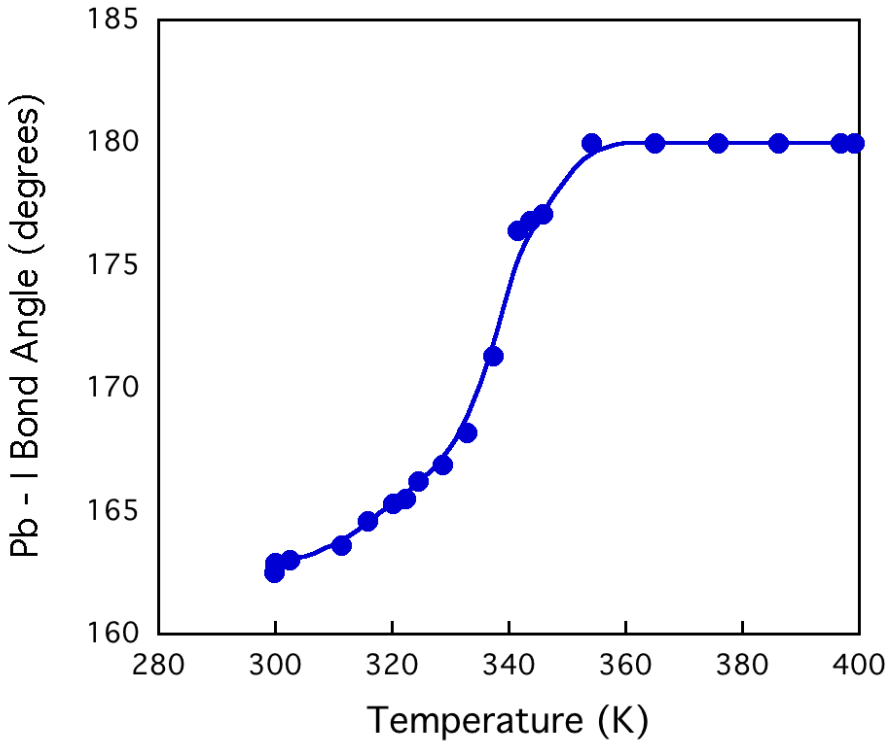

Figure 19. Variation of the Pb – I bond angle as a function of temperature in prototypical $MAPbI_3$ derived from powder XRD refinement

Single crystal x-ray diffraction of the prototypical $MAPbI_3$ was carried out at room temperature on a Rigaku Oxford Diffraction SuperNova diffractometer. The diffraction measurement was carried out as a full sphere scans at 290 K using the copper wavelength. Unlike powder crystal diffraction, single crystal diffraction allowed for absolute atomic positions and therefore more accurate refinement of the bond angles and lengths of the sample. The refinement reinforced the results from the powder diffraction data. The crystal was assigned to the I4/m space group with parameters a = b = 8.8756 Å c = 12.6517 Å and $\alpha = \beta = \gamma = 90°$. In correspondence with the powder diffraction results, the single crystal refinement the unit cell volume was found to be 996.654 $Å^3$. The single crystal x-ray diffraction data allowed for refinement of the Pb – I – Pb dihedral bond angles, which were found to average 163.993° in the tetragonal phase. In contrast, in the high-temperature $Pm\bar{3}m$ phase this angle increased to an average of 180.00° due to adjustment of the octahedral cages which become aligned along the c axis in order to maintain the cubic structure.

3.3. Annealing of Prototypical $MAPbI_3$

The quality – more specifically the morphology, crystallinity and defect concentration at grain boundaries – of inorganic-organic halide perovskites materials may be enhanced using thermal treatments such as annealing.[22] For example, the Oswald ripening process which utilises annealing in order to promote favourable oriented grains has proven to be a successful thermal treatment.[22] The time, temperature and environment in which the crystals are annealed are fundamental to the intrinsic properties of the material. There is a fine balance between enhancing the properties of the $MAPbI_3$ perovskite and decomposition at high temperatures. The purpose of the study is to distinguish changes to the prototypical $MAPbI_3$ structure when annealed over various temperatures and environments.

3.3.1. Low Temperature Annealing

Initially, research was focused on how the $MAPbI_3$ structure transformed as a function of temperature. $MAPbI_3$ (0.5 g) was placed in a ceramic crucible and heated for 24 hours in an oven at temperatures of 60°C, 80°C, 100°C and 200°C. Standard annealing temperatures reported in previous studies are in the range of 80-100°C, this was used as a benchmark to encompass common annealing conditions and also conditions outside of the normal range. The second means of manipulation of the $MAPbI_3$ crystals, with the degradation susceptibility of the structure in mind, was to anneal the crystals in an inert vacuum environment for comparison with the standard atmospheric environment samples. $MAPbI_3$ (0.5 g) was placed in a quartz vacuum tube of diameter 6mm, which was evacuated to $P = 1\ x\ 10^{-3}$ torr and sealed. The samples were heated for 24 hours in an oven. Annealing was performed at temperatures of 60°C, 80°C, 100°C and 200°C.

Sample	Temperature (°C)	Pressure (torr)	Time (hours: minutes)	Environment
$MAPbI_3$-60	60	Atmospheric	24:00	Atmospheric conditions
$MAPbI_3$-80	80	Atmospheric	24:00	Atmospheric conditions
$MAPbI_3$-100	100	Atmospheric	24:00	Atmospheric conditions
$MAPbI_3$-200	200	Atmospheric	24:00	Atmospheric conditions
$MAPbI_3$-V60	60	$1\ x\ 10^{-3}$	24:00	Vacuum
$MAPbI_3$-V80	80	$1\ x\ 10^{-3}$	24:00	Vacuum
$MAPbI_3$-V100	100	$1\ x\ 10^{-3}$	24:00	Vacuum
$MAPbI_3$-V200	200	$1\ x\ 10^{-3}$	24:00	Vacuum

Table 2. Table of low temperature samples and respective annealing conditions

Powder XRD diffraction measurements were taken of the synthesised crystals at the BM31 beamline over the temperatures 100 – 400 K.

Following annealing treatment at 200°C the $MAPbI_3$-200 sample had fully degraded, evident by a distinct yellow colouring of the crystalline sample. In contrast, the vacuum annealed $MAPbI_3$-V200 sample remained intact, as confirmed by refinement of the powder XRD profile. The results are consistent with studies which state degradation of the $MAPbI_3$ structure occurs when oxygen is present. Iodine atoms donate electrons to the oxygen molecules, resulting in iodide anions that produce free radicals. The free radicals are capable of deprotonating the MAI cation therefore leaving behind pure PbI_2. $MAPbI_3$ decomposes at annealing temperatures of approximately 120 °C, however in this case it was evident that the absence of O_2 in the vacuum annealed sample allowed for increased stability of the sample up until at least 200 °C and therefore could allow for annealing at higher temperatures to be achieved whilst supressing degradation of the sample.

Atom	*x*	*y*	*z*	Occ.
Pb1	0.0	0.0	0.0	0.96
Pb2	0.0	0.0	0.5	0.94
I1	0.0	0.0	0.25	1.0
I2	0.2209	0.2791	0.5	1.0
N1/C1	0.5577418	-0.0635307	0.2926486	0.349

Table 3. Refined atomic positions and occupancy derived from the refined powder XRD profile of the $MAPbI_3$-V200 sample. Powder XRD carried out at the BM31 beamline over the temperatures 100 – 400 K.

3.3.2. High Temperature Vacuum Annealing

Consequential to the findings of the low temperature annealing methods it was decided to carry out annealing of the prototypical $MAPbI_3$ under a vacuum environment, at higher temperatures outside of the conventional range. $MAPbI_3$ (0.5 g) was placed in a ceramic crucible inside a glass vacuum tube ($P = 1\ x\ 10^{-3}$ torr) and heated for 1.5 hours. This process was repeated at every 5°C interval over the temperature range 280 – 320 °C. Due to the increased heating temperatures, a percentage of the crystal sample had decomposed to produce PbI_2. This was immediately apparent on removal from the oven due to the bright yellow colour of the crystals. In order obtain a clear diffraction pattern the PbI_2 was separated from the perovskite phase. Samples did not require further washing with solvents. Subsequent to annealing the samples, a black gelatinous residue was seen to accumulate in the glass vacuum tube which was believed to contain some form of MAI. Raman spectroscopy was carried out on the sample which confirmed it was a carbon containing compound.

Sample	Temperature (°C)	Pressure (torr)	Time (hours: minutes)	Environment
$MAPbI_3$-V280	280	$1\ x\ 10^{-3}$	1:30	Vacuum
$MAPbI_3$-V285	285	$1\ x\ 10^{-3}$	1:30	Vacuum
$MAPbI_3$-V290	290	$1\ x\ 10^{-3}$	1:30	Vacuum
$MAPbI_3$-V300	295	$1\ x\ 10^{-3}$	1:30	Vacuum
$MAPbI_3$-V305	300	$1\ x\ 10^{-3}$	1:30	Vacuum
$MAPbI_3$-V310	310	$1\ x\ 10^{-3}$	1:30	Vacuum
$MAPbI_3$-V315	315	$1\ x\ 10^{-3}$	1:30	Vacuum
$MAPbI_3$-V320	320	$1\ x\ 10^{-3}$	1:30	Vacuum

Table 4. Summary of high temperature annealing samples and respective annealing conditions

Powder x-ray diffraction patterns were measured at room temperature on a X'pert[3] powder x-ray diffractometer for all high temperature vacuum annealed samples. It was observed that at elevated annealing temperatures, peak splitting in the XRD profile occurred, associated with the presence of more than one structural phases within the sample. Unlike the prototypical $MAPbI_3$ which remains in the tetragonal phase at room temperature, Rietveld refinements revealed that the vacuum annealed samples presented increasing phase fraction of a simple cubic $Pm\bar{3}m$ phase over the annealed temperature range. Refinements determined that although the lowest temperature sample $MAPbI_3$-V280 was refined as a tetragonal structure, substantial decrease in scattering intensity at 23.3° in the $MAPbI_3$-V305 profile indicated a phase transition. Based on the splitting pattern observed in the XRD profiles it was predicted that the two phases were present simultaneously in varying phase fractions rather than in isolation, thus a tetragonal structural model was used to refine all samples.

(a)

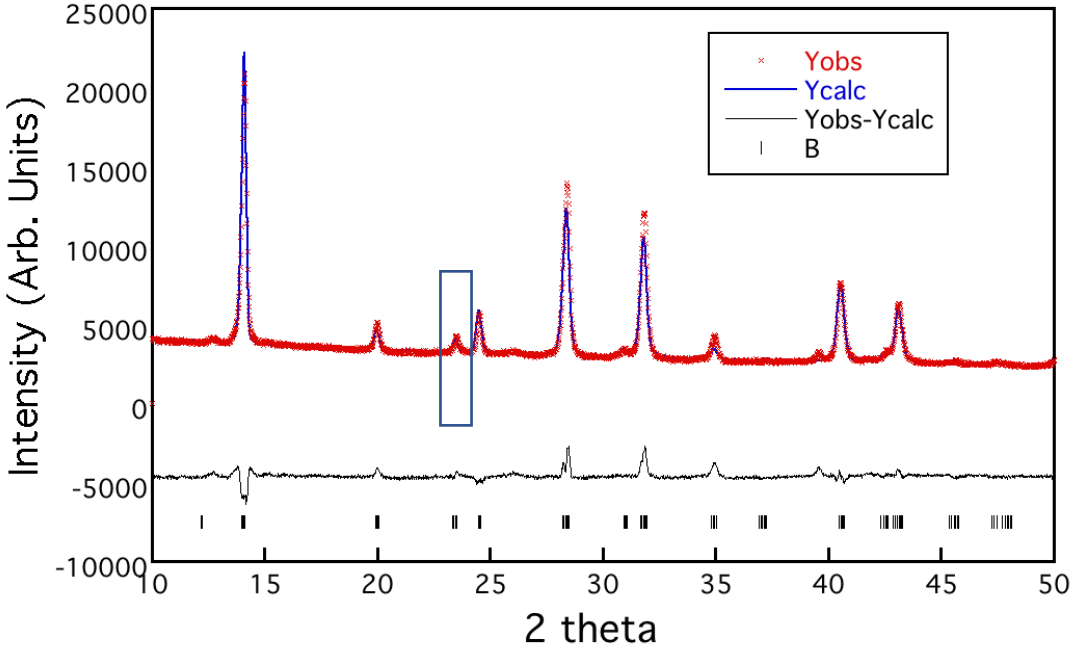
Yobs
Ycalc
Yobs-Ycalc
B
Intensity (Arb. Units)
2 theta
25000
20000
15000
10000
5000
0
-5000
-10000
10
15
20
25
30
35
40
45
50

(b)

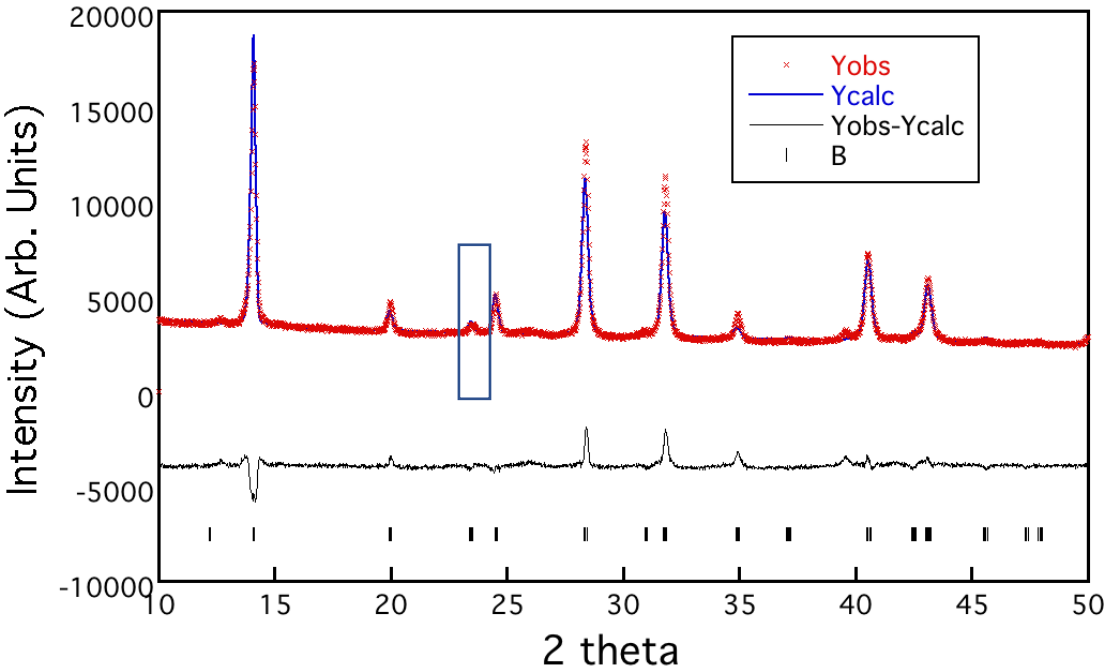
Yobs
Ycalc
Yobs-Ycalc
B
Intensity (Arb. Units)
2 theta
20000
15000
10000
5000
0
-5000
-10000
10
15
20
25
30
35
40
45
50

(c)

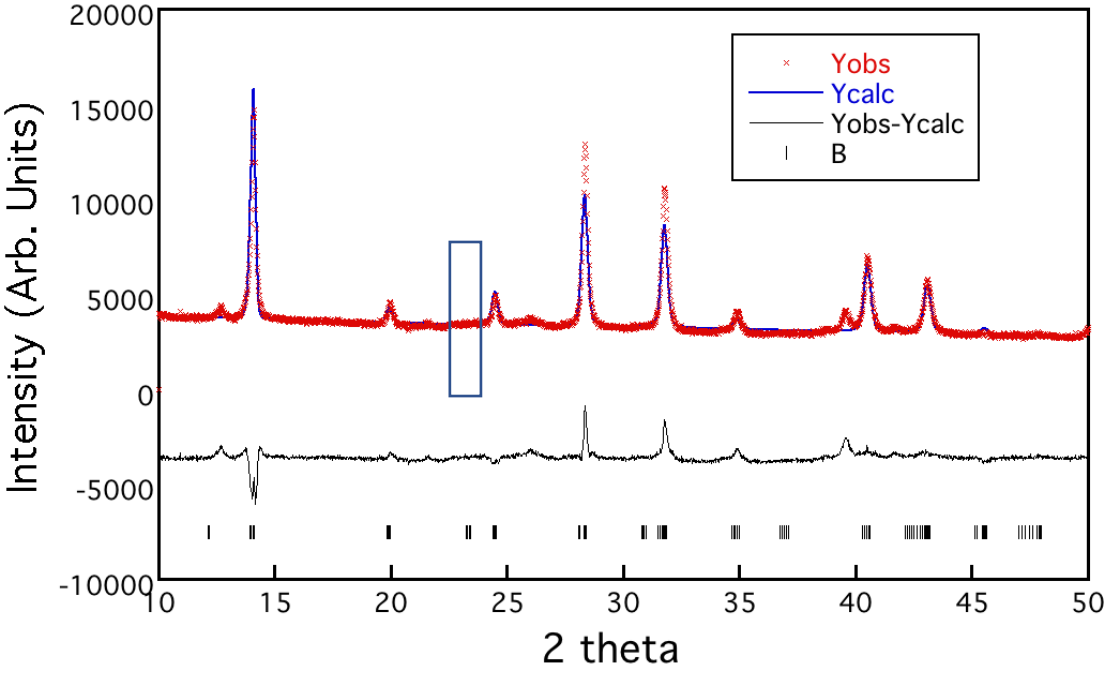

(d)

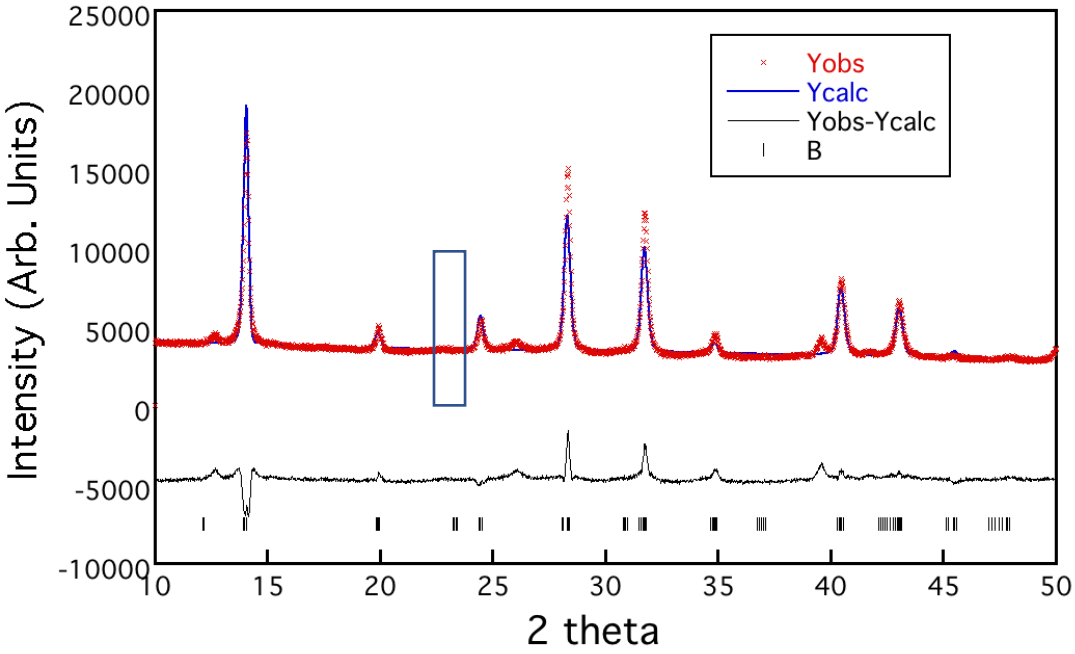

Figure 20. X-ray diffraction profile for samples (a) $MAPbI_3$-V285 (b) $MAPbI_3$-V295 (c) $MAPbI_3$-V305 (d) $MAPbI_3$-V315, indicating suppression of the (211) indexed peak. Powder XRD carried out at on the X'pert[3] diffractometer.

Atom	***x***	***y***	***z***	**Occ.**
Pb1	0.0	0.0	0.25	1.0
Pb2	0.0	0.0	0.5	1.0
I1	0.0	0.0	0.0	1.0
I2	0.2153	0.2847	0.5	0.25
N1/C1	0.55828	-0.0630	0.29260	0.25

Table 5. Atomic positions and occupancies of the refined $MAPbI_3$-V280 sample

Atom	***x***	***y***	***z***	**Occ.**
Pb1	0.0	0.0	0.25	1.0
Pb2	0.0	0.0	0.5	1.0
I1	0.0	0.0	0.0	1.0
I2	0.2366	0.2634	0.5	0.25
N1/C1	0.55828	-0.0630	0.29260	0.25

Table 6. Atomic positions and occupancies of the refined $MAPbI_3$-V315 sample

Refinements indicate that the cubic fraction of the sample increases and the average structure of the perovskite is gradually transformed away from the initial tetragonal phase towards a higher symmetry cubic phase. The refinements reveal that when the annealing temperature of each sample is increased the ratio of the indexed reflections (211):(022) decreases consistently, as the (211) peak is supressed. Sample $MAPbI_3$-V305 displays absence of the (211) reflection altogether, consistent with peak splitting of high angle suppression seen in the cubic phase of prototypical $MAPbI_3$. The suppression of the 211 peak over the annealing temperature range is displayed in Figure 20 and Figure 21.

Prototypical $MAPbI_3$ is able to transform to the cubic phase at high temperatures and pressures, but it has proven difficult to stabilise the phase at room temperature. The cubic phase

demonstrated by the high temperature vacuum annealed samples remains post annealing process, demonstrating that the thermal treatment stabilises the cubic phase at room temperatures and is not dependent on thermal conditions seen in the prototypical sample where the cubic transition occurs only at T > 345 K .

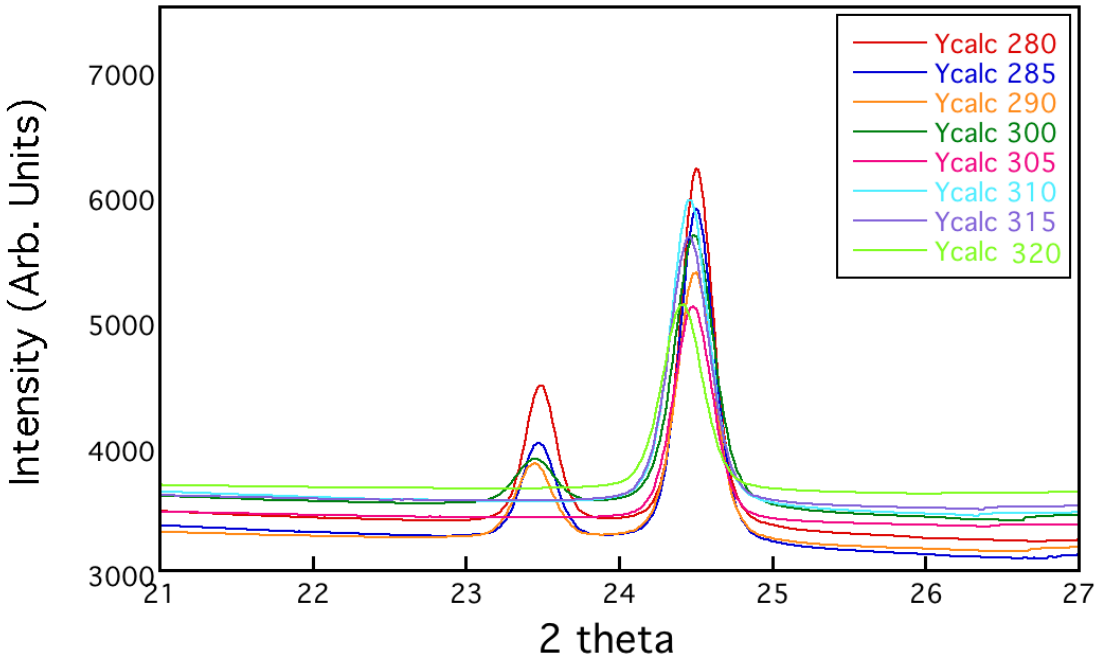

Figure 21. Powder XRD profile in the range of 21 – 27 2θ, outlining the suppression of the 211 reflection in $MAPbI_3$ as a function of annealing temperature

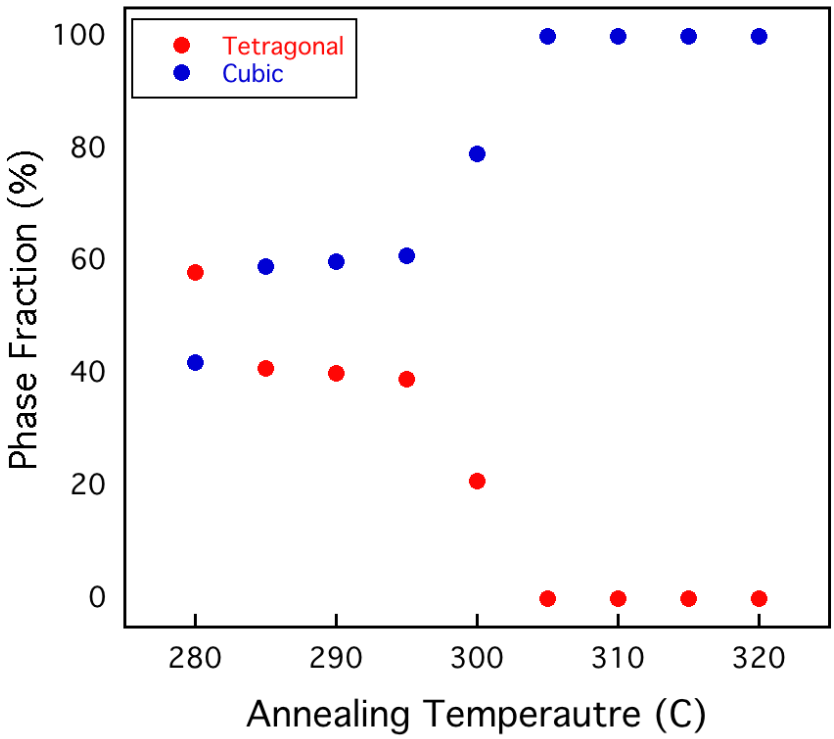

Figure 22. Phase fraction of tetragonal:cubic phase corresponding to the vacuum annealed $MAPbI_3$ samples over the annealing temperatures 280°C – 320°C derived from sequential Rietveld refinements

Using the Rietveld refinements of each sample the phase fraction as a function of annealing temperature was determined and are outlined in Figure 22. The phase fraction, deduced from sequential Rietveld refinement revealed the ratio of cubic:tetragonal phase within the powder sample. The results summaries that the structure deviates away from the tetragonal phase, becoming a more predominantly cubic arrangement as the annealing temperature is increased. Samples $MAPbI_3$-V305, $MAPbI_3$-V310, $MAPbI_3$-V315 and $MAPbI_3$-V320 were refined against 100% cubic structures, indicating that the minimum annealing temperature required for the cubic structural form is T = 305 °C. The transition to a cubic structure is dependent upon the degree of tilt of the PbI_6 cages. The refinements suggest that as the annealing temperature is increased the degree of octahedral tilt decreases as the cages became aligned along the c axis. The Pb – I – Pb bond angles increased consistently from 164.12° in sample $MAPbI_3$-V280 to 174.32° in sample $MAPbI_3$-V315, closer to the ideal cubic model of 180°, as displayed in Figure 23. On comparison with the prototypical $MAPbI_3$, the Pb – I – Pb bond angles of $MAPbI_3$-V315 at room temperature are significantly increased as a result of the post synthesis

thermal annealing. Interestingly, the analogous perovskite $CsPbBr_3$ transitions to a cubic perovskite phase at T = 315 °C.

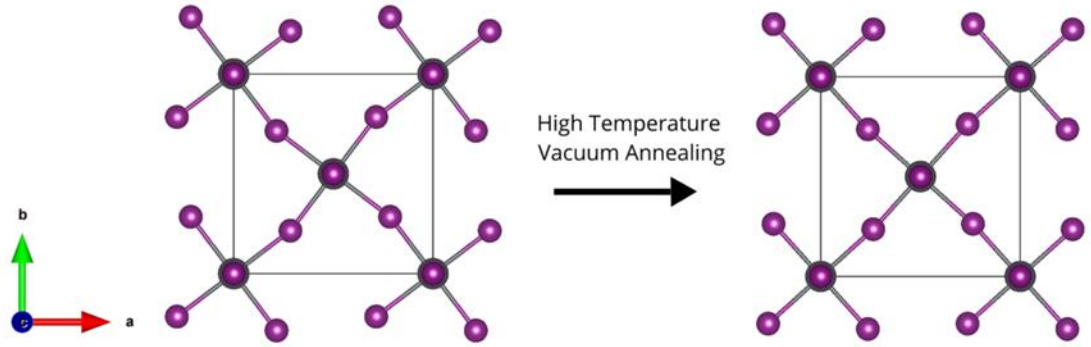

Figure 23. Structural model of the increasing Pb – I – Pb bond angles in samples $MAPbI_3$-V280 (left) and $MAPbI_3$-V315 (right)

The cubic transition is believed to occur as a direct result of the annealing process which facilitates a disproportionation reaction, liberating MAI. It is possible that by heating the $MAPbI_3$ sample to a threshold temperature, T>305°C, the structure of the organic cation begins to deteriorate and eventually releases MAI from the crystal lattice. The black viscous residue found in the annealing tube during synthesis is assumed to contain some composition of methyl ammonium iodide. As a result of this annealing process the subsequent lattice will possess MAI deficiencies. Through alteration of the cation occupying the A site the degree of distortion of the lead-iodide framework will be directly affected, resulting in structural modifications of the prototypical $MAPbI_3$ crystal.

The distortion of the octahedral is associated with the sterics of the A cation, and therefore with the Goldschmidt's tolerance factor. As the methyl ammonium cation deteriorates upon high temperature vacuum annealing it is likely that the ionic radius increases. As a consequence, the Goldschmidt's tolerance factor moves towards the ideal perovskite and respectively Pb-I-Pb bond angles become increased, until the point at which they reach the cubic phase, corresponding to Glazer notation $a^0a^0a^0$. A DTF study undertaken to explore atomic-scale insights inot halide perovskites reported in its findings that the PbI_3 octahedra distortion is associated to the chemical nature of the MA cation rather than its size.[74] It is evident that in

this case, the chemical properties of the MA cation play a role in its deterioration and hence may be an additional influence on the octahedral tilt.

Although the cubic phase has been shown to exist up to temperatures of 320°C, the higher temperatures fundamentally causes the lattice to collapse and decompose into MAI and PbI_2. This was both visibly evident from increasing percentage of the characteristic yellow PbI_2 phase within the sample and the diffraction peaks indexed as PbI_2. Synthesis of the 320°C sample resulted in the lowest sample yield of 32.38% due to removal of the decomposed phase. The black residue formed in the annealing tube was confirmed a carbon containing by-product of this process via Raman spectroscopy analysis, however the identity and composition was not determined. Interestingly, in a similar high temperature vacuum assisted study of $MAPbI_3$, the generation of a MACl by-product was reported.

3.3.3. Conclusions

In summary, conducting high temperature vacuum annealing has successfully promoted alteration to the prototypical $MAPbI_3$ structure at annealing temperature T>305°C, confirmed through PXRD refinements. Contradictory to the transitions seen in prototypical $MAPbI_3$, powder x-ray diffraction data has determined that high temperature (305°C <T<320°C) vacuum annealed $MAPbI_3$ is able to exist as a stable cubic phase not defined by the temperature constraint T > 345K. It has been shown by means of powder x-ray diffraction that the tetragonal phase of prototypical $MAPbI_3$, seen as ambient temperatures, is suppressed as a function of increasing annealing temperatures, eventually yielding a cubic phase at annealing temperature T>305°C.

The cubic structure displays higher symmetry, defined by the increased alignment of the polyhedral cages which comprise the perovskite framework. Refinement of the Pb-I-Pb bond angles has concluded that the bond angles are increased compared to those in prototypical $MAPbI_3$, associated with small coherent displacements of the halide ions. The degree of distortion of the lead-halide cages are correlated with the intrinsic stability of the structure, and therefore it is likely that the high temperature (305°C <T<320°C) vacuum annealed sample displays increased stability compared with prototypical $MAPbI_3$.

According to the Shockley-Queisser theory, the tetragonal-cubic transition of prototypical $MAPbI_3$ occurs within the operating range of the cell, therefore it is disruptive to the photovoltaic behaviour of the cell due to effects on the band gap.[2]. By stabilising the high temperature annealed cubic phase over the operating range, it eradicates the transition and may potentially increase performance of the cell.

This research has revealed that the transitions of the $MAPbI_3$ perovskite are not limited to the 3 distinct phases and that in fact there are more subtle variations in phases over smaller temperature ranges. The research has also outlined that such phases can be dependent on the choice of synthetic route. Interestingly these phases may prove to have more favourable properties, such as enhanced stability, than the prototype.

3.4. Interstitial Iodine Incorporation into Prototypical $MAPbI_3$

Whilst addition of interstitial iodine into the $MAPbI_3$ structure has been achieved experimentally, the presence and dynamics of these species, and consequences of such on the photovoltaic ability of the material remain far from understood. The mobility of interstitial iodine molecules has been considered heavily involved in the photovoltaic mechanism of $MAPbI_3$ but little is known of how additional iodine incorporation via interstitial sites affects the material structurally. Studies exposing $MAPbI_3$ to high partial pressures of iodine have previously been conducted yet concluded no significant structural variation. Interestingly elevation of the electrical properties such as electrical conductivity were observed. The studies displayed clear limitations in the experimental method, such as temperature range, pressure range and the environment of the $MAPbI_3$ crystals, yet had not been further developed. Initially this was the incentive to further explore iodine incorporation in the $MAPbI_3$ structure.

3.4.1. Annealing of Prototypical $MAPbI_3$ in I_2 Vapour

Exposure of $MAPbI_3$ crystals to I_2 vapour, was carried out over a range of temperatures and durations, and with a range of I_2 concentrations. The sample was annealed within a small quartz tube (Diameter = 6mm), which was evacuated at a Schleck line. A temperature range above to the boiling point of I_2 was chosen for annealing. Prior to all annealing processes the quartz tubes were heated to 100 °C for 10 minutes in order to eradicate water vapour present inside the tube that could interfere with the annealing process.

$MAPbI_3$ (0.35 g) was placed in a quartz tube, followed by iodine resublimed crystals (0.10 g). The tube was evacuated to $P = 1\ x\ 10^{-3}$ torr and sealed before being heated for 1.5 hours in a tube furnace. This process was repeated at temperatures of 200 °C, 250 °C, 260 °C, 270 °C, 280 °C, 290 °C and 300 °C. All crystals were subsequently washed with diethyl ether (5-7 mL) and collected via vacuum filtration.

Sample	Temperature (°C)	Pressure (torr)	Time (hours: minutes)	Environment
$MAPbI_3$-IV200	200	$1\ x\ 10^{-3}$	1:30	Vacuum, I_2 vapour
$MAPbI_3$-IV250	250	$1\ x\ 10^{-3}$	1:30	Vacuum, I_2 vapour
$MAPbI_3$-IV260	260	$1\ x\ 10^{-3}$	1:30	Vacuum, I_2 vapour
$MAPbI_3$-IV270	270	$1\ x\ 10^{-3}$	1:30	Vacuum, I_2 vapour
$MAPbI_3$-IV280	280	$1\ x\ 10^{-3}$	1:30	Vacuum, I_2 vapour
$MAPbI_3$-IV290	290	$1\ x\ 10^{-3}$	1:30	Vacuum, I_2 vapour
$MAPbI_3$-IV300	300	$1\ x\ 10^{-3}$	1:30	Vacuum, I_2 vapour

Table 7. Summary of I_2 vapour annealed samples and respective annealing conditions

Powder x-ray diffraction measurements were taken at the BM31 beamline at the ESRF Facility for the $MAPbI_3$-IV200 sample, using λ=0.956 at 290K. The Rietveld refinement profile is displayed in Figure 24. On comparison of the prototypical $MAPbI_3$ powder x-ray diffraction profile there is an obvious adjustment in peak positions, where the prototypical $MAPbI_3$ displayed split peaks the I_2 treated sample displayed distinctive single peaks which are characteristic of a cubic structural profile of a higher symmetry phase. This is most apparent in the (200) reflection at 17.3674°, and further emphasised by the absence of intensity at 14.5237° and 19.0478° in the $MAPbI_3$-IV200 sample, as demonstrated in Figure 25. The diffraction profile contained impurities indexed as PbI_2 and NH_4PbI_3.

The profile confirmed evolution of the prototypical tetragonal phase to a stabilised cubic structural phase had been achieved at ambient temperatures by means of the I_2 annealing process. The crystal phase itself has not been reported in prior literature and is therefore being considered a newly discovered crystal phase of the parent $MAPbI_3$ perovskite.

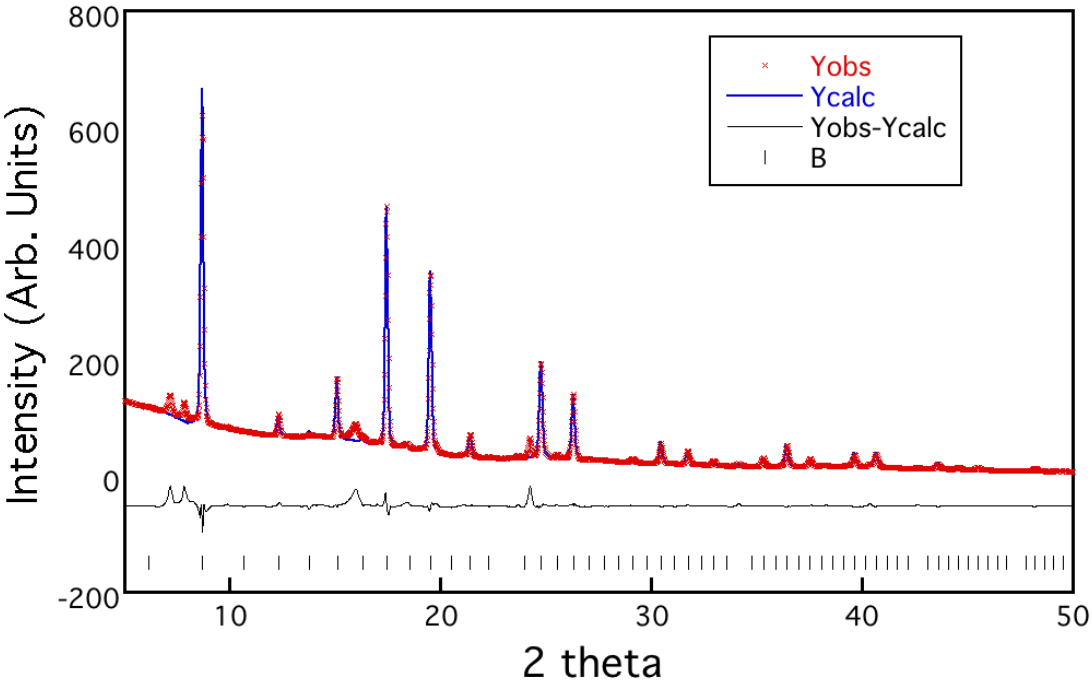

Figure 24. Powder x-ray diffraction profile of the $MAPbI_3$-IV200 sample obtained at the BM31 beamline at the ESRF facility at 290 K

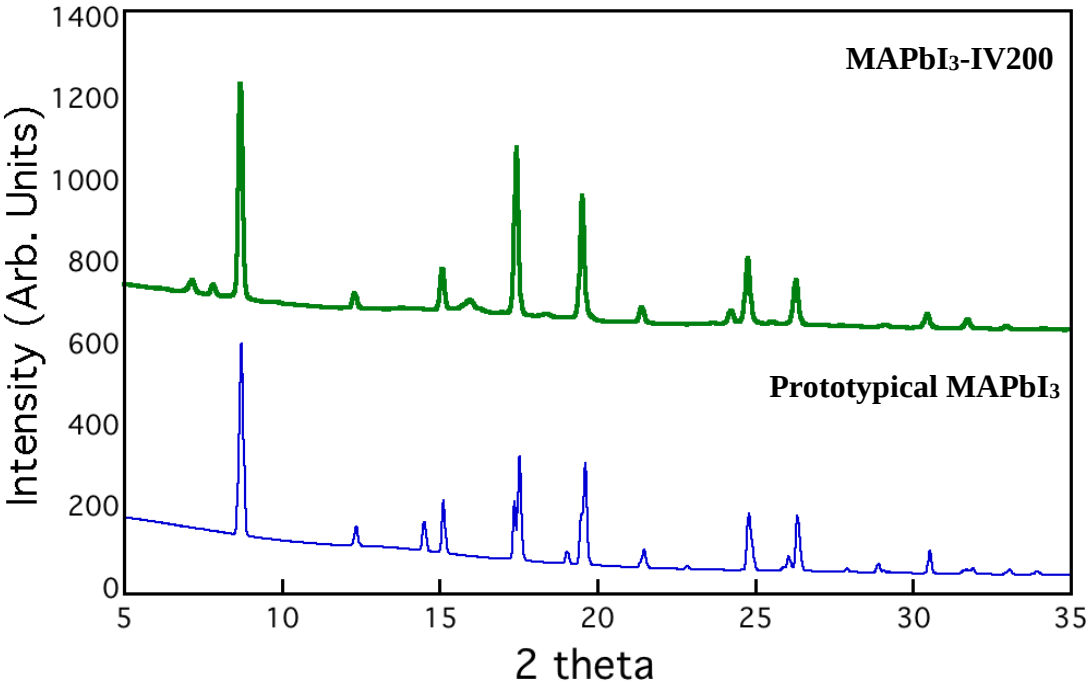

Figure 25. Comparison of the $MAPbI_3$-IV200 sample and prototypical $MAPbI_3$ and untreated phase powder x-ray diffraction spectra between the ranges 5 – 35 2θ

X-ray single crystal diffraction was also measured at the BM01 ESRF Facility at 290K for the $MAPbI_3$-IV200 sample. Structural refinement was carried out using SHELXS and SHELXL software. On refinement, and comparison of several space groups, the crystal was concluded to belong of the $Im\bar{3}$ space group with the lowest R factor. The single crystal diffraction profile confirmed the presence of a simple cubic lattice with interstitial iodine sites. Lattice parameters were as follows a = b = c = 6.3273 Å and $\alpha = \beta = \gamma = 90°$. The atom positions and occupancies of the $Im\bar{3}$ cubic phase are displayed in Table 8.

Atom	**x**	**y**	**z**	**Occ**
Pb1	0.25000	0.25000	0.75000	0.950
I1	0.28800	0.50000	0.73400	0.180
N2	0.02000	0.50000	1.00000	0.680
C2	0.02000	0.50000	1.00000	0.680
C1	0.56400	0.50000	0.50000	0.200
N1	0.56400	0.50000	0.50000	0.200
I2B	0.22000	0.50000	0.73400	0.067
I2A	0.25690	0.50000	0.76950	0.710

Table 8. Atomic positions and occupancies of the refined $MAPbI_3$-IV200 sample powder XRD profile

Under ordinary conditions at T = 290 K the $MAPbI_3$ structure would exist in the tetragonal phase, and it has not before been reported in a cubic phase at ambient temperatures or pressures. It has been shown by variable temperature powder XRD that in the case of the prototypical $MAPbI_3$ the transitional temperature for the tetragonal-cubic transition occurs at T=345K. In contrast, the $MAPbI_3$-IV200 crystal was designated to the $Im\bar{3}$ cubic space group at 290K confirming a phase transition from the prototypical tetragonal structure to a cubic structure at T>345K as a result of the I_2 annealing treatment.

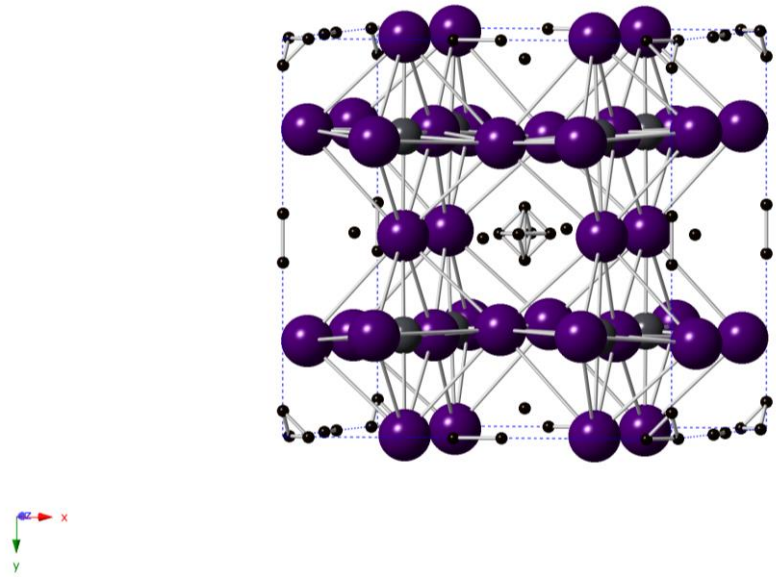

Figure 26. Structural model of $MAPbI_3$-IV200 deduced from powder x-ray diffraction refinement at 290 K carried out at BM01

It was additionally discovered by means of single crystal x-ray diffraction data of the $MAPbI_3$-IV200 crystal that the MA^+ cations significantly differ from the prototypical cubic phase. The single crystal refinement determined that in the $MAPbI_3$-IV200 sample the MA^+ cations had adopted highly ordered positions along a single crystallographic axis as opposed to the typically observed disordered and dynamic MA^+ groups within the prototypical $MAPbI_3$ crystal system. The single crystal refinement determines that the ordered methyl ammoniums are positioned on each vertex of the unit cell and an additional ordered methyl ammonium cation occupies the centre vacancy of the cell. The difference in MA^+ dynamics is likely a consequence of the reduced occupancy of the MA^+ site in the $MAPbI_3$-IV200 sample.

Despite the refinement confirming the cubic structure of the crystal, the arrangement of the lead-iodide octahedral do not conform to the expected 180.00° Pb – I – Pb bond angles as seen in the prototypical $MAPbI_3$ cubic structure. In this case the polyhedral cages within the $MAPbI_3$ cubic cell are unusually distorted and display a degree of tilt, with a bond angle of 172.27°. It is thought that the methyl ammonium cation arrangement and distribution within the crystal lattice is a fundamental influence of the lead-halide bond angles and distances and hence the geometric stability of the system.

Single crystal refinement of the $MAPbI_3$-IV200 sample revealed two interstitial iodine sites, I2A and I2B, which are not present in the prototypical $MAPbI_3$. Results suggest transition to the cubic phase allows introduction of these interstitial iodine atoms, influenced by high partial pressures of iodine during the annealing process, which occupy methyl ammonium deficient sites. The methyl ammonium deficient sites are thought to be created on annealing the crystal above a high temperature threshold.

The incorporation of iodine interstitial molecules is known to subsequently generate deep hole trapping mechanisms within the structure. The refinement outlines the interstitial sites, with the I2A site displaying the highest occupancy of 0.710. The unusual defect properties of the $MAPbI_3$ crystal when iodine interstitial sites are present have previously been linked to their PCE. Literature suggests that the iodine interstitial sites introduce a shallow trap state close to the valence band.[75] This facilitates migration of the holes into the valence band before they have the opportunity for recombination with electrons, resulting in longer lifetimes for the deep hole trapping phenomena, and hence minimising energy losses. [75]

Variable temperature x-ray diffraction carried out at the BM31 beamline at the ESRF Facility over the temperatures 100 – 400 K revealed an additional thermal transition in the $MAPbI_3$-IV200 sample. Refinements over the temperature range revelaed at temperatures above 315K an alternative cubic unit cell was adopted by the $MAPbI_3$ structure. At 315K a high temperature cubic structure was observed that took the form of a larger cubic system designated to the space group $Pm\bar{3}m$. The lattice parameters were refined as a = b = c = 12.6047 Å and $\alpha = \beta = \gamma = 90°$ and an increased unit cell volume of 2002.62 $Å^3$. This second cubic phase exhibited a distinct difference from the prototypical $MAPbI_3$ cubic phase and initial $MAPbI_3$-IV200 simple cubic phase due to the substantial increase in the *a* lattice parameter.

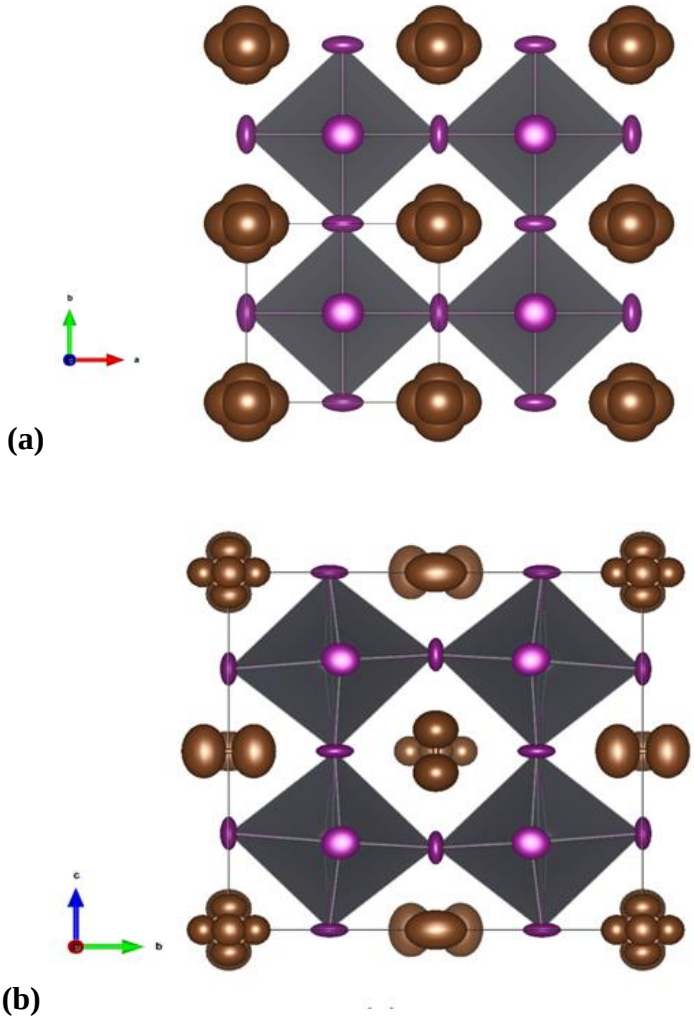

Figure 27. Structural model of the $MAPbI_3$-IV200 sample in (a) the $Im\bar{3}$ cubic phase present at ambient temperature and (b) the $Pm\bar{3}m$ cubic phase at T>315K derived from single crystal XRD

	Prototypical $MAPbI_3$	**Prototypical $MAPbI_3$**	**$MAPbI_3$-IV200**	**$MAPbI_3$-IV200**
Crystal System	Tetragonal	Cubic	Cubic	Cubic
Stability Range (K)	T < 345 K	T > 345 K	270 K – 315 K	T > 315 K
Space group	*I4/m*	$Pm\bar{3}m$	$Im\bar{3}$	$Pm\bar{3}m$
Lattice Parameters (Å)	a = b = 8.8756 c = 12.6517	a = b = c = 6.3123	a = b = c = 6.3273	a = b = c = 12.6047
Cell Volume (Å^3)	994.577	251.5142	253.3137	2002.61996

Table 9. Comparison of the average structural parameters of the prototypical $MAPbI_3$ transitions and the $MAPbI_3$-IV200 transitions

The various temperature powder diffraction measurements confirm the formation of the two cubic polymorphs of the $MAPbI_3$-IV200 crystal structure. The powder x-ray diffraction profiles also established that over the temperature range of 100 K to 400 K the crystal exhibited no transition to a tetragonal phase at any intermittent temperature, indicating that the iodine annealing process provides an irreversible transition from prototypical $MAPbI_3$ to the new phase. It is likely that the iodine stabilisation inhibits or entirely prevents structural transitions to the tetragonal phase. A summary of the prototypical $MAPbI_3$ and the $MAPbI_3$-IV200 sample are outlined in Table 9. The table identifies the transition of $MAPbI_3$-IV200 sample from simple cubic to large cubic at 315K and the tetragonal-cubic transition of the prototypical phase at 345K. The lead-iodide octahedra in the large cubic phase displayed further disorder compared with the simple cubic $Im\bar{3}$ phase.

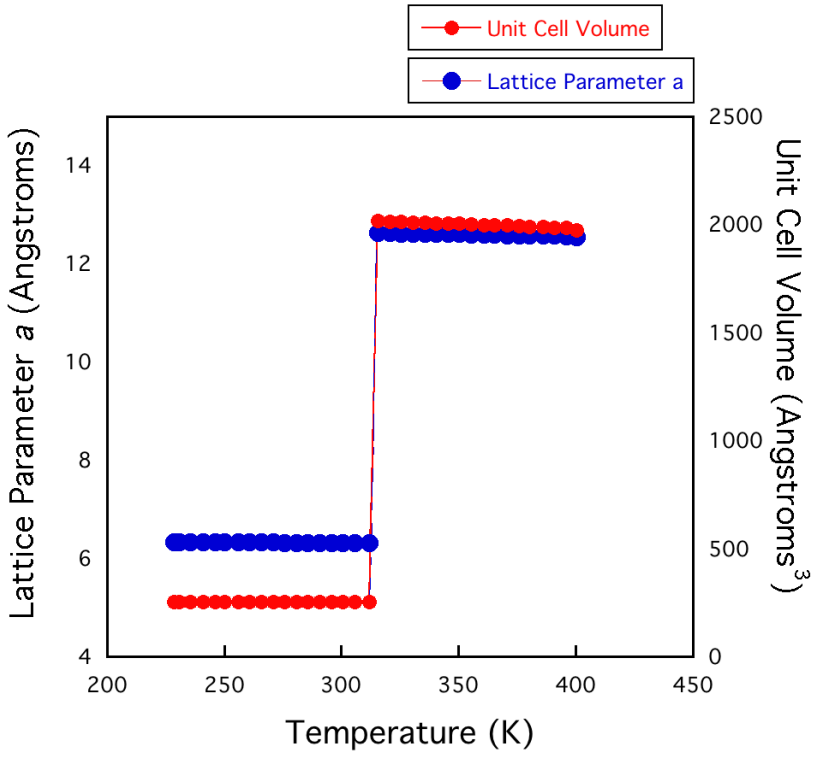

Figure 28. Lattice parameter a and unit cell volume of $MAPbI_3$-IV200 as a function of temperature over the range 240 – 400 K

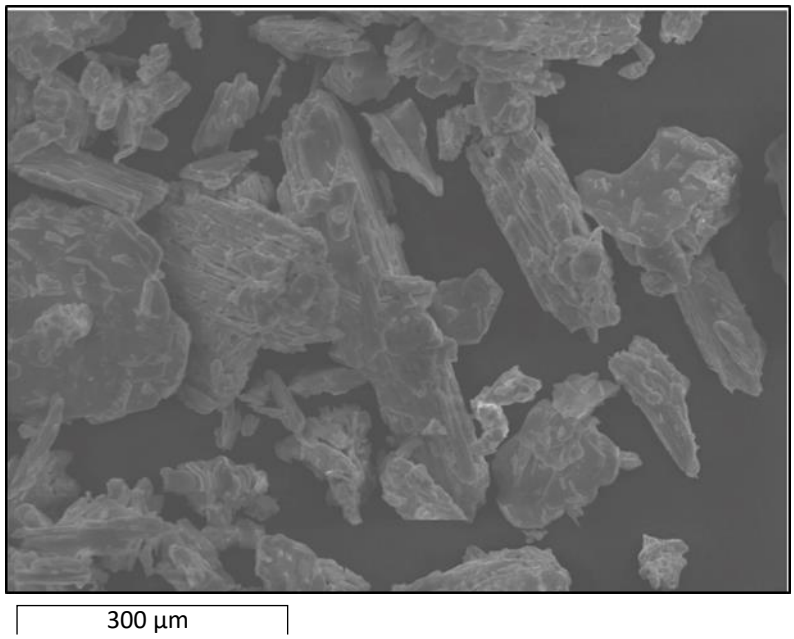

Figure 29. Scanning electron microscopy (SEM) imaging of the $MAPbI_3$-IV200 sample, following annealing treatment with iodide vapour at 200°C

Scanning electron microscopy was used for imaging of the $MAPbI_3$-IV200 sample displayed in Figure 29. Post iodine annealing the crystals remained black and iridescent in colour yet the morphology of the crystals varied greatly from those seen in prototypical $MAPbI_3$. Post annealing treatment the $MAPbI_3$-IV200 crystal facets lacked defined shape, and displayed greater variation of both shape and size compared with the more uniform prototypical sample. The crystals appeared to be coated with an impurity despite washing in solvents.

Neutron powder diffraction of the $MAPbI_3$-IV200 sample was measured on the Powgen diffractometer at the Oak Ridge Facility, however it was decided to omit the results from the study as the high degree of background noise lead to difficulties in refinement of the profile. The background noise is likely as a result of the large neutron scattering caused by the hydrogen atoms within the methyl ammonium group.

3.4.2. Conclusions

To conclude, the present study concerned with vacuum assisted annealing in iodine vapour has proven extremely successful in inducing structural change in the prototypical $MAPbI_3$. In fact, by means of this post synthetic treatment a new structural phase was synthesised, confirmed by both single crystal and powder x-ray diffraction. Unlike prototypical $MAPbI_3$, the structural phase $MAPbI_3$-IV200 is stable as a cubic $Im\bar{3}$ lattice at ambient temperatures.

The structure has additional interstitial iodine sites, which are correlated with a deep hole trapping mechanism, potentially warranting superior PCEs compared with prototypical $MAPbI_3$.[75] It was also deduced through single crystal refinement that the $MAPbI_3$-IV200 sample displays highly ordered MA^+ cations. With less dynamic, highly ordered MA^+ sites it is probable that the structure itself becomes less susceptible to degradation from external molecules compared with the prototypical $MAPbI_3$.

Furthermore, a transition at T>315 K to a second larger cubic $Pm\bar{3}m$ phase was identified. A similar cubic phase has been published by Jiang *et al*. which attributes the stabilisation of the cubic phase to the high-pressure synthesis, made possible by use of a diamond anvil press which facilitates pressures in excess of 0.8 GPa.[76] The transition is reversible by removing the mechanical pressure. This study has presented an alternate means of stabilisation of an

analogous cubic phase, through chemical vapour with the additional benefit of stability at room temperatures and pressure, without the need for complex and expensive equipment. It is often observed that chemical pressure can stabilise mechanical pressure, which is believed to be the mechanism behind the formation of the $Pm\bar{3}m$ cubic phase in this case.

3.5. Further Chemical Manipulation of Prototypical $MAPbI_3$

Further to the above methods, additional means of chemical manipulation of the prototypical $MAPbI_3$ were carried out as outlined below. In some cases it was decided to introduce other elements into the annealing process.

3.5.1. High Temperature Annealing In The Presence Of Zinc

$MAPbI_3$ (0.50 g) and Zn (0.5 g) were placed at opposite ends of a ceramic crucible inside of a glass vacuum tube. The tube was evacuated ($P=1x10^{-3}$ torr) and heated for time intervals of 30 minutes, 1 hour, and 2 hours at temperatures of 200 °C, 250 °C and 300 °C.

Sample	Temperature (°C)	Pressure (torr)	Time (hours: minutes)	Environment
$MAPbI_3$-ZnV200	200	$1\,x\,10^{-3}$	0:30	Vacuum
$MAPbI_3$-ZnV200-I	200	$1\,x\,10^{-3}$	1:30	Vacuum
$MAPbI_3$-ZnV200-II	200	$1\,x\,10^{-3}$	2:00	Vacuum
$MAPbI_3$-ZnV250	250	$1\,x\,10^{-3}$	0:30	Vacuum
$MAPbI_3$-ZnV250-I	250	$1\,x\,10^{-3}$	1:30	Vacuum
$MAPbI_3$-ZnV250-II	250	$1\,x\,10^{-3}$	2:00	Vacuum
$MAPbI_3$-ZnV260	300	$1\,x\,10^{-3}$	0:30	Vacuum
$MAPbI_3$-ZnV260-I	300	$1\,x\,10^{-3}$	1:30	Vacuum
$MAPbI_3$-ZnV260-II	300	$1\,x\,10^{-3}$	2:00	Vacuum

Table 10. Summary of Zn annealed samples and respective annealing conditions

X-ray diffraction measurements concluded a significant structural shift was observed, as it appeared that the originally tetragonal $MAPbI_3$ had transformed to the cubic phase compound and had not transitioned back to the tetragonal phase despite cooling to room temperature. On reviewing the method, zinc was removed from the reaction and it was deduced that it was the high temperature, vacuum environment as outlined in the previous section which was responsible for the transition.

3.5.2. Annealing In Bromide Vapour

Following the success of the iodine vapour induced phase, annealing process using alternative halogens were considered. Annealing on exposure to bromine vapour was subsequently carried out, using lower temperatures that corresponded to bromines boiling point.

$MAPbI_3$ (0.5 g) was placed in a quartz tube (d=6mm), followed by bromine (0.2 mL). Before being placed under vacuum (P = $1x10^{-2}$ torr), the tube was placed in a dewar of liquid nitrogen, and intermediately throughout the evacuating process to freeze the bromine liquid and prevent loss. The sample was then heated at 80°C for 1 hour. The resulting orange crystals were washed with diethyl ether (5 mL) and collected via vacuum filtration using a Buchner flask.

Sample	**Temperature (°C)**	**Pressure (torr)**	**Time (hours: minutes)**	**Environment**
$MAPbI_3$-BrV80	80	$1\ x\ 10^{-2}$	1:00	Vacuum

Table 11. Summary of Br annealed sample and respective annealing conditions

Incorporation of bromine to the annealing process failed to show any noteworthy deviations from the general $MAPbI_3$ structure, expect for discolouration of the characteristic black $MAPbI_3$ crystals.

3.5.3. Annealing Under a Nitrogen Atmosphere

The final method of manipulation involved annealing the crystals in under a nitrogen atmosphere.

$MAPbI_3$ (0.5 g) was placed in a ceramic crucible within a glass vacuum tube which was evacuated and then purged with nitrogen. The purging procedure was repeated three times. The sample was then heated for 1.5 hours at 200°C. In order to stabilise the pressure from inside the glass tube a bubbler was connected.

Sample	Temperature (°C)	Pressure (torr)	Time (hours: minutes)	Environment
$MAPbI_3$-N200	200	$1\ x\ 10^{-3}$	1:30	Inert, N_2

Table 12. Summary of N_2 annealed sample and respective annealing conditions

Annealing of the perovskite under a nitrogen purged environment did not produce a structural transformation of the $MAPbI_3$ phase.

4. Overall Conclusions

The results of the study has outlined synthesis of the prototypical $MAPbI_3$ perovskite and two successful attempts at inducing structural changes in prototypical $MAPbI_3$ perovskite through chemical manipulation techniques.

Overall the study revealed two fundamental findings; on high temperature vacuum annealing a structural tetragonal-cubic transition occurs and secondly that on annealing $MAPbI_3$ with exposure to iodide vapour an amorphisation occurs resulting in a thermally stable cubic phase at ambient temperatures. The $MAPbI_3$-VI200 phase has not previously been reported in literature so is being defined as a new phase. The optimal annealing conditions are summarised below.

Sample	**Temperature**	**Time (hours:minutes)**	**Refined Phase**
Prototypical	-	-	Tetragonal
$MAPbI_3$-VI200	200°C	1.5 hours	Cubic
$MAPbI_3$-V305	305-320°C	1.5 hours	Cubic (predominantly)

Table 13. Summary of the refined phases of prototypical $MAPbI_3$ with $MAPbI_3$-VI200 and $MAPbI_3$-V305, outlining annealing conditions and respective crystal phases

The use of vacuum assisted annealing at temperatures which were unusually high for $MAPbI_3$ annealing processes allowed for a lasting structural transition to be induced. The transition from a tetragonal *I4/m* phase to simple cubic $Pm\bar{3}m$ phase is correlated to the alignment of the octahedral cages, a vital component of the structure of the cell which is heavily associated with the intrinsic stability of the $MAPbI_3$ structure. The emergence of this phase transition under simple and cost-effective annealing conditions presents great potential for the tuning of the stability of the $MAPbI_3$ cell and similar families of perovskites. The stability of such structures has long been a concern for the commercial applications in the solar sector, hence insight into a mechanism whereby the stability may be improved is crucial to their success.

Equally, iodine vapour has previously been used in exploration of the $MAPbI_3$ parent structure although a phase transition had not be observed. Synthesis in this case resulted in the transition from the prottypical *I4/m* $MAPbI_3$ tetragonal structure to a cubic $Im\bar{3}$ structure. Unlike the prototypical $MAPbI_3$ structure, the MA^+ sites were found to be highly ordered and the crystal presented defects in the form of interstitial iodine sites. These sites may be linked to mechanisms such as deep-hole trapping and may also contribute to widening of the band gap.

A similar structure has been presented in the literature, which requires high mechanical pressures exerted via a diamond anvil press in order to be synthesised.[76] The method put forward in this project does not require such strenuous routes of synthesis and as such is a more practical and inexpensive alternative to achieve the desired phase, warranting the further research into the methods outlined in this study.

The characterisation techniques, most fundamentally the single crystal analysis, have led to greater understanding of how annealing environments can modify vital components of the cell, such as the degree of octahedral tilt, ordering of the system, distribution of crystal defects or the band gap structure. These insights are fundamental to the engineering of the structure, and most crucially, the chemical properties of the cell including the photovoltaic, ferroelectric and magnetic functionalities. The project has worked towards refining new design concepts for $MAPbI_3$ crystals with the tuneable properties.

4.2. Future Work

The most fundamental route of investigation which was not carried out during this project due to time constraints but which would provide great insight is QEM Band Gap Analysis. Band gap analysis would confirm if the $MAPbI_3$-IV200 sample demonstrated a wider bandgap compared with the prototypical $MAPbI_3$. Band gap analysis would give further insight into how the iodine interstitials affect the band gap and consolidate previous DFT studies which state that they play a role in deep hole trapping phenomena. Further to this, the stability of the new phases must be determined in order to confirm the theory that the stability of the cell is increased by the cubic transitions. The stability may be investigated by TGA analysis which will give insight on the new phase, relative to the prototypical structure.

Quasielastic neutron scattering could be beneficial in gaining a more detailed insight into the dynamics of the methyl ammonium cation, and how the motion of the cation is affected subsequent to the annealing methods implemented in this study. Solid state NMR would be complimentary to this, aiding additional analysis into the ordering of the MA^+ cation within the structure. The quasielastic neutron route of analysis may also provide information on the crucial iodine dynamics, in particular the mechanisms of the interstitial sites which are thought to be fundamental to the amorphisation in the $MAPbI_3$-IV200 sample.

Low temperature x-ray diffraction is essential in order to determine if the two distinct cubic phases observed are in fact permanent, irreversible evolutions. It would be useful to carry out diffraction in lower temperature regions.

References

[1]. C.C. Stoupos, D.H. Cao, D.J. Clark, J. Young, J.M. Rondinelli, J.I. Jang, J.T. Hupp & M.G. Kanatzidis, 'Ruddlesden−Popper Hybrid Lead Iodide Perovskite 2D Homologous Semiconductors' Chem. Matter, 2016, 28, 8

[2]. Y. Yuan, T. Li, Q. Wang, J. Xing, A. Gruverman & J. Huang, 'Anomalous photovoltaic effect in organic-inorganic hybrid perovskite solar cells' Science Advances, 2017, 3, 3

[3]. World Energy Council, World Energy Resources Full Report, 2016, 14-31

[4]. M. M. Halmann, M. Steinberg, 'Greenhouse Gas Carbon Dioxide Mitigation' Science and Technology, 1998, 2-8

[5]. K. Thomas, E. Trenberth. 'Modern global climate change' Science, 2003, 302, 1719-1723

[6]. C. Le Quéré., Earth Syst. Sci. Data, 2018, 10, 2141–2194

[7]. International Energy Agency, World Energy Outlook Report, 2018

[8]. World Energy Council, World Energy Resources Full Report, 2010

[9]. I. B. Fridleifsson, 'Geothermal energy for the benefit of the people' Renewable and sustainable energy reviews, 5, 3, 2001, 299-312

[10]. J. Hill, E. Nelson, D. Tilman, S. Polasky & D. Tiffany, 'Environmental, economic, and energetic costs and benefits of biodiesel and ethanol biofuels' Proceedings of the National Academy of Sciences of the United States of America, 103, 2006

[11]. P. Hofmann, Solid State Physics: An Introduction, John Wiley & Sons, 2015

[12]. L.E. Smart, and E.A. Moore, 'Solid state chemistry: An Introduction', CRC press, 2016.

[13]. Cui, Tongxiang & Lv, Ruitao & Huang, Zheng-Hong & Chen, Shuxiao & Zhang, Zexia & Gan, Xin & Jia, Yi & Li, Xinming & Wang, Kunlin & Wu, Aoran & Kang, Feiyu, Enhanced efficiency of graphene/silicon heterojunction solar cells by molecular doping, Journal of Materials Chemistry, 2013, 5736-5740

[14]. W. Shockley & H. J. Queisser, 'Detailed Balance Limit of Efficiency of pn Junction Solar cells' Journal of Applied Physics, 1961, 21, 501, 510-513

[15]. S. Rühle 'Tabulated values of the Shockley–Queisser limit for single junction solar cells' Solar Energy, 2016, 130, 139-147.

[16]. Yurduseven, Okan & Smith, D. & Pearsall, Nicola & Forbes, Ian, A transparent solar patch antenna for 2.4/2.5 GHz WLAN-WiMAX applications, 2012

[17]. K. Bernard, and J. Brédas, 'Organic photovoltaics' Energy & Environmental Science, 2009, 2, 251-261.

[18]. Martin A Green, Third generation photovoltaics: solar cells for 2020 and beyond, Physica E: Low-dimensional Systems and Nanostructures,Volume 14, 2002, Issues 1–2,

[19]. N. Park, 'Perovskite solar cells: an emerging photovoltaic technology' Materials today, 2015, 18, 65-72

[20]. K. Sharma, V. Sharma and S. S. Sharma. 'Dye-sensitized solar cells: fundamentals and current status.' Nanoscale research letters, 2018, 13, 381.

[21]. Iftikhar, H., Sonai, G. G., Hashmi, S. G., Nogueira, A. F., & Lund, P. D, 'Progress on electrolytes development in dye-sensitized solar cells.' Materials, 2019, 12, 1998

[22]. Wang, B., Wong, K. Y., Xiao, X., & Chen, T, 'Elucidating the reaction pathways in the synthesis of organolead trihalide perovskite for high-performance solar cells' Scientific reports, 2015, 5, 10557

[23]. Zhao, Xing, and N. Park. 'Stability issues on perovskite solar cells' Photonics, 2015, 2, 4

[24]. Jiang, S., Fang, Y., Li, R., Xiao, H., Crowley, J., Wang, C., ... & Fang, J, 'Pressure-Dependent Polymorphism and Band-Gap Tuning of Methylammonium Lead Iodide Perovskite' Angewandte Chemie International Edition, 2016, 55, 6540-6544.

[25]. Kawamura, Yukihiko, H. Mashiyama, and K. Hasebe. 'Structural study on cubic-tetragonal transition of CH3H3PbI3' Journal of the Physical Society of Japan, 2002, 71, 1694-1697.

[26]. Bertolotti, F., Protesescu, L., Kovalenko, M. V., Yakunin, S., Cervellino, A., Billinge, S. J, 'Coherent nanotwins and dynamic disorder in cesium lead halide perovskite nanocrystals.' ACS nano, 2017, 11, 3819-3831.

[27]. Goldschmidt, V. Moritz.'Die gesetze der krystallochemie' Naturwissenschaften, 1926, 14, 477-485.

[28]. P.M. Woodward, 'Octahedral tilting in perovskites. I. Geometrical considerations' Acta Crystallographica Section B: Structural Science, 1997, 53, 32-43

[29]. C.J. Howard, and H. T. Stokes, 'Group-theoretical analysis of octahedral tilting in perovskites.' Acta Crystallographica Section B: Structural Science, 1998, 54, 782-789

[30]. Whitfield, P. S., Herron, N., Guise, W. E., Page, K., Cheng, Y. Q., Milas, I., & Crawford, M. K, 'Structures, phase transitions and tricritical behavior of the hybrid perovskite methyl ammonium lead iodide' Scientific reports, 2016, 6, 35685

[31]. F. Shojaei and Wan-Jian Yin, 'Stability Trend of Tilted Perovskites' The Journal of Physical Chemistry, 2018, 122, 15214-15219

[32]. Quarti, C., Mosconi, E., Ball, J. M., D'Innocenzo, V., Tao, C., Pathak, S, 'Structural and optical properties of methylammonium lead iodide across the tetragonal to cubic phase transition: implications for perovskite solar cells.' Energy & Environmental Science, 2016, 9, 155-163.

[33]. F.F. Targhi, Y.S. Jalili and F. Kanjouri, ‘MAPbI3 and FAPbI3 perovskites as solar cells: Case study on structural, electrical and optical properties.’ Results in Physics, 2018, 10, 616-627.

[34]. Weller, M. T., Weber, O. J., Henry, P. F., Di Pumpo, A. M., & Hansen, T. C., ‘Complete structure and cation orientation in the perovskite photovoltaic methylammonium lead iodide between 100 and 352 K’ Chemical communications, 2015, 51, 4180-4183

[35]. Chen, T., Foley, B. J., Ipek, B., Tyagi, M., Copley, J. R., Brown, C. M, ‘Rotational dynamics of organic cations in the CH3NH3PbI3 perovskite’, Physical Chemistry Chemical Physics, 2015, 17, 31278-31286

[36]. Kawamura, Yukihiko, H. Mashiyama, and K. Hasebe, ‘Structural study on cubic-tetragonal transition of CH3NH3PbI3.’, Journal of the Physical Society of Japan, 2017, 71, 1694-1697

[37]. Z. Shi and H.J. Ahalapitiya, ‘Perovskites-based solar cells: A review of recent progress, materials and processing methods’, Materials, 2018, 11, 729

[38]. Yuan, Yongbo, and Jinsong Huang. "Ion migration in organometal trihalide perovskite and its impact on photovoltaic efficiency and stability." Accounts of Chemical Research 49.2 (2016): 286-293.

[39]. Minns, J. L., Zajdel, P., Chernyshov, D., Van Beek, W., & Green, M. A, ‘Structure and interstitial iodide migration in hybrid perovskite methylammonium lead iodide’ Nature communications, 2017, 8, 1-5

[40]. J. Azpiroz et al. ‘Defect migration in methylammonium lead iodide and its role in perovskite solar cell operation’, Energy & Environmental Science, 2015, 8, 2118-2127

[41]. M. Du ‘Efficient carrier transport in halide perovskites: theoretical perspectives’, Journal of Materials Chemistry, 2014, 2, 9091-9098

[42]. C. Lin, S. Li, W. Zhang, C. Shao & Z. Yang, 'Effect of Bromine Substitution on the Ion Migration and Optical Absorption in MAPbI3 Perovskite Solar Cells: The First Principles Study', American Chemical Society, 2018, 1, 1374-1380

[43]. Yin, X.; Yao, Z.; Luo, Q.; Dai, X.; Zhou, Y.; Zhang, Y.; Zhou, Y.; Luo, S.; Li, J.; Wang, N, High Efficiency Inverted Planar Perovskite Solar Cells with Solution-Processed NiOx Hole Contact. ACS Appl. Mater. Interfaces 2017, 9 (3), 2439–2448.

[44]. Yang, H., Zhang, J., Zhang, C., Chang, J., Lin, Z., Chen, D. & Hao, Y,'Effects of annealing conditions on mixed lead halide perovskite solar cells and their thermal stability investigation.', Materials, 2017, 10, 837

[45]. Jiang, Y., Pan, L., Wei, D., Li, W., Li, S., Yang, S. E. & Chen, Y. 'The modified multi-step thermal annealing process for highly efficient MAPbI3-based perovskite solar cells.', Solar Energy, 2018, 174, 218-224

[46]. Ava, T. T., Al Mamun, A., Marsillac, S., & Namkoong, G, A review: thermal stability of methylammonium lead halide based perovskite solar cells, Applied Sciences, 2019, 9, 188

[47]. Smecca, E., Numata, Y., Deretzis, I., Pellegrino, G., Boninelli, S., Miyasaka, T.& Alberti, A, Stability of solution-processed MAPbI 3 and FAPbI 3 layers, Physical Chemistry Chemical Physics, 2016, 18, 13413-13422

[48]. Sutton, R. J., Eperon, G. E., Miranda, L., Parrott, E. S., Kamino, B. A., Patel, J. B., ... & Snaith, H. J, 'Bandgap-tunable cesium lead halide perovskites with high thermal stability for efficient solar cells.' Advanced Energy Materials, 2016, 6, 150-245

[49]. L. Meng, J. You, and Yang Yang. 'Addressing the stability issue of perovskite solar cells for commercial applications.' Nature communications, 2018, 9, 5265

[50]. Starkholm, Allan, Lars Kloo, and P. H. Svensson. 'Polyiodide Hybrid Perovskites: A Strategy To Convert Intrinsic 2D Systems into 3D Photovoltaic Materials.' ACS Applied Energy Materials, 2018, 2, 477-485

[51]. Hao, F., Stoumpos, C. C., Cao, D. H., Chang, R. P., & Kanatzidis, M. G, Lead-free solid-state organic–inorganic halide perovskite solar cells' Nature Photonics, 2014, 8, 489

[52]. Lyu, M., Yun, J. H., Cai, M., Jiao, Y., Bernhardt, P. V., Zhang, M. & Wang, L, 'Organic–inorganic bismuth (III)-based material: A lead-free, air-stable and solution-processable light-absorber beyond organolead perovskites." Nano Research, 2016, 9, 692-702

[53]. Song, T. B., Chen, Q., Zhou, H., Jiang, C., Wang, H. H., Yang, Y. M & Yang, Y. 'Perovskite solar cells: film formation and properties.' Journal of Materials Chemistry A, 2015, 3, 9032-9050

[54]. Ha, S. T., Liu, X., Zhang, Q., Giovanni, D., Sum, T. C., & Xiong, Q, 'Synthesis of Organic–Inorganic Lead Halide Perovskite Nanoplatelets: Towards High-Performance Perovskite Solar Cells and Optoelectronic Devices.' Advanced Optical Materials, 2014, 2, 838-844

[55]. C.C. Stoupos, D.H. Cao, D.J. Clark, J. Young, J.M. Rondinelli, J.I. Jang, J.T. Hupp & M.G. Kanatzidis, 'Ruddlesden−Popper Hybrid Lead Iodide Perovskite 2D Homologous Semiconductors', Chem. Matter, 2016, 28, 8

[56]. A. Guinier, X-ray diffraction in crystals, imperfect crystals, and amorphous bodies. Courier Corporation, 1994

[57]. Y. Waseda, E. Matsubara, and K. Shinoda, X-ray diffraction crystallography: introduction, examples and solved problems. Springer Science & Business Media, 2011

[58]. Advanced Certificate of Diffraction Birkbek College University of London, URL: http://pd.chem.ucl.ac.uk/pdnn/inst1/xrays, Date accessed: August 2019

[59]. R.E. Dinnebier and S.J.L. Billinge. 'Principles of powder diffraction', Powder Diffraction Theory and Practice, 2008, 19

[60]. Online Dictionary of Crystallography, URL: http://reference.iucr.org/dictionary/Reciprocal_space, Date accessed: August 2019

[61]. C. Kittel, Introduction to solid state physics. Vol. 8. New York: Wiley, 1976

[62]. M.T. Dove, 'Structure and dynamics: an atomic view of materials' Oxford University Press, 2003, 1

[63]. M. Yan and A. Gibaud., 'On the intersection of grating truncation rods with the Ewald sphere studied by grazing-incidence small-angle X-ray scattering.', Journal of Applied Crystallography, 2007, 40, 1050-1055.

[64]. Science and Technology Facilities Council ISIS Neutron & Muon Source, URL: https://www.isis.stfc.ac.uk/Pages/Neutron-diffraction.aspx, Date accessed: August 2019

[65]. R.A. Young, 'The rietveld method.' International union of crystallography, 5, 1993

[66]. G.L. Squires, Introduction to the theory of thermal neutron scattering, Cambridge University Press, 2012

[67]. Institute of Physics, Neutron Scattering Report, 2018

[68]. S. Elliott, The physics and chemistry of solids, Wiley, 1998

[69]. Malvern PANalytical, X'pert3 Powder Diffraction Brochure, 2014

[70]. D. McKie and C. McKie, 'Essentials of crystallography', 1986

[71]. Aglient Technologies, X-ray Crystallography Systems Brochure, 2012

[72]. The European Synchrotron Facility SNB Diffractometer, URL: https://www.esrf.eu/UsersAndScience/Experiments/CRG/BM01/bm01b/the-snb-diffractometer, Date Accessed: August 2019

[73]. Huq, A., Hodges, J. P., Gourdon, O., & Heroux, L., Powgen: A third-generation high-resolution high-throughput powder diffraction instrument at the Spallation Neutron Source, Z. Kristallogr. Proc, 2011, 1, 127-135

[74]. Ghosh, D., Smith, A. R., Walker, A. B., & Islam, M. S, Mixed a-cation perovskites for solar cells: atomic-scale insights into structural distortion, hydrogen bonding, and electronic properties, Chemistry of Materials, 2018, 30.15, 5194-5204.

[75]. Li, Wei & Liu, Jin & Bai, Fu-Quan & Song, Ming-Xing & Prezhdo, Oleg, Hole Trapping by Iodine Interstitial Defects Decreases Free Carrier Losses in Perovskite Solar Cells: A Time-Domain Ab Initio Study. ACS Energy Letters, 2017, 2

[76]. Jiang, S., Fang, Y., Li, R., Xiao, H., Crowley, J., Wang, C., White, T.J., Goddard III, W.A., Wang, Z., Baikie, T. and Fang, J. Pressur,e-Dependent Polymorphism and Band-Gap Tuning of Methylammonium Lead Iodide Perovskite. Angewandte Chemie, 2016, 128, 6650-6654.